ABSTRACT

Title of Dissertation: ADVANCES IN THE APPLICATION OF SUPERCONDUCTING AND PHOTONIC CIRCUITS TO MICROWAVE RADIOMETERS

Charles Josiah Turner
Doctor of Philosophy, 2023

Dissertation Directed by: Professor Thomas E. Murphy
Department of Electrical & Computer Engineering

In the fields of radio astronomy and remote sensing, there are application-driven requirements for wideband radiometers, hyperspectral spectrometers, and Radio Frequency Interference (RFI) mitigation. This work investigates the implementation of superconducting filters for RFI mitigation in ground-based radio astronomy where cryogenic cooling is available. It also explores the feasibility of implementing Photonic Integrated Circuits (PICs) in spaceborne radiometers. Spaceborne instruments have strict size, weight, and power consumption (SWaP) requirements. PICs are intrinsically wideband and offer significant SWaP benefits for enhanced performance in radiometers. This thesis presents three topics in technology development for the advancement of radiometers.

The first topic is the development of a thin-film, high-temperature superconductor (HTS) notch filter to reject a local, high-power, RFI signal. The resonator topology was devised to minimize the necessary coupling between the transmission line and resonators. As demonstrated

through measurements, this filter has an operating frequency range of 2-12 GHz and provides over 50 dB of rejection around 9.41 GHz. The measured maximum insertion loss is 0.6 dB in the lower pass-band and 2 dB in the upper pass-band, which can be reduced through improved packaging and operating the device at lower temperatures. This device currently demonstrates the largest 50-dB-rejection stop-band reported in literature for thin-film HTS filters at 4.3% fractional bandwidth.

The second topic is a stochastic, non-linear, power-response model with supporting laboratory measurements for a photonics-enabled, heterodyne, microwave radiometer. The measurements are taken from a single-channel test device and the results can be applied to improve the design and simulation accuracy of a multi-channel spectrometer. This model is tested by comparing the measured gain of a photonic down-converter (PDC) under an applied continuous wave microwave signal versus an adjustable microwave noise source. The PDC consists of a dual-drive Mach Zehnder Modulator with a microwave local oscillator (LO) used for down-conversion of the microwave carrier signal. Using these results, the dynamic range of the proposed instrument is quantified with improved accuracy.

The third topic is the demonstration of thermo-reflectance microscopy (TRM) on a polymer-based photonic device. A spaceborne, photonics-enabled, microwave radiometer needs to survive and operate in a space environment. Measuring the thermal profile of PICs is essential for creating more environmentally-robust designs, but many feature sizes fall below the diffraction limit for traditional infrared thermography. TRM offers a means of measuring thermal profiles by using visible-wavelength light to reduce the diffraction limit and achieving sub-micron spatial resolutions. Photonic Wire Bond (PWB) is an important component for coupling different PICs without requiring active optical alignment between chips. Although TRM has been tested before

with semiconductors, it has not been demonstrated before on PWB. These results demonstrate the possibility of using TRM to test complete, multi-material PIC devices.

Advances in the Application of Superconducting and Photonic Circuits to Microwave Radiometers

by

Charles Josiah Turner

Dissertation submitted to the Faculty of the Graduate School of the
University of Maryland, College Park in partial fulfillment
of the requirements for the degree of
Doctor of Philosophy
2023

Advisory Committee:
Professor Thomas E. Murphy, Chair/Advisor
Professor Yanne K. Chembo
Professor Thomas M. Antonsen, Jr.
Dr. Mark A. Stephen
Professor Andrew I. Harris, Dean's Representative

Dedication

To my wife Mireille and my children Elijah, Lucas, and Finley for their love and patience during this pursuit.

Acknowledgments

During my undergraduate and graduate tours, my spouse and I entered parenthood and are now raising three children. To support my family, I had to work part-time while in undergrad and full-time as a grad student. Balancing work, family, and school has by far been the most challenging and demanding endeavour of my life. I was only able to succeed thanks to the support, patience, and understanding that I received from my family and friends along the way.

I want to thank Thomas Murphy and Andrew Harris for a long history of their mentorship. I met Thomas Murphy in 2014 when he became my undergraduate mentor and Andrew Harris shortly after when I received my first exposure to radio astronomy and radiometry in his course. Whether it was in one of their courses or figuring out how to pursue research and funding, I felt greatly supported through the time that they committed to me. It was an especially challenging time to continue research during the restrictions we all faced at the peak of COVID-19, and still I felt fully enabled to continue pursuing lab work thanks to them. Thank you to Thomas Antonsen for supporting me to conduct research as an undergrad, encouraging me to go to grad school, and serving on my committee. Thank you also to Yanne Chembo for providing support and test equipment to complete testing of the photonic wire bond, as well as serving on my committee. Also from the University of Maryland, I'd like to thank Melanie Prange and Emily Irwin for providing fantastic support and making sure I had little to worry about outside of the research itself.

I also want to thank Mark Stephen for advising me while I worked at NASA Goddard Space Flight Center. I learned a lot from him and without the opportunities he provided, I would not have entered the world of microwave photonics. He was the first to guide me through the process of research proposals and its through him that I have felt confident to operate more independently. I want to thank Paul Racette for connecting me with Mark and getting me involved in these opportunities at NASA, as well as both Paul and Jeffrey Piepmeier for taking the time to talk with me about radiometry and passing on their knowledge. Also from NASA I'd like to thank Jared Lucey, Matthew Fritts, Negar Ehsan, U-yen Kongpop, Berhanu Bulcha, Gordon Chin, and Carrie Anderson for their time and mentorship. I'd especially like to thank Michael Coon for saying just the right thing, at just the right time, to ensure I would see this research to completion.

As if supporting a family and working full-time wasn't enough a challenge, my family and I decided to up-root and move to New Hampshire in the last few years of this research. This was a joyful decision as it brought us closer to my wife's family, but I became greatly uncertain if I would be able to commit the time to complete the degree requirements and graduate. At BAE Systems, I would to thank Mackenzie Van Camp, Sachin Dekate, and John Kelly for providing continued support, funding, and encouragement to finish. I also want to thank Zachary Hileman for providing advice while I pursued additional funding and finish this work.

Finally, I'd like to thank my close friend Chase Kielbasa. As a fellow military veteran, he is no stranger to hearing complaints ("the salt"). Still, he listened to me complain on multiple occasions for 7 years about anything there is to complain about, which helped me get it off my chest and move on. He's been more patient and understanding than he's needed to be, and has always been a great source of support and encouragement during this process.

Table of Contents

List of Tables

List of Figures

List of Abbreviations

ACS	Auto-Correlator Spectrometer
ADS	Advance Design System (Keysight)
AOS	Acousto-Optical Spectrometer
ASIC	Application-Specific Integrated Circuit
CCD	Charge-Coupled Device
CMOS	Complementary Metal-Oxide Semiconductor
CTS	Chirp Transform Spectrometer
CWS	Continuous Wave Signal
DC	Direct Current
DFB	Distributed Feed-Back
EM	Electromagnetic
EOM	Electro-Optic Modulator
GGAO	Goddard Geophysical Astronomical Observatory
HFSS	High Frequency Structural Simulator
HTS	High Temperature Superconductor
HYMPI	Hyperspectral Microwave Photonic Instrument
IR	Infrared
ITU	International Telecommunication Union
LD	Laser Diode
LED	Light-Emitting Diode
LNA	Low Noise Amplifier
MRR	Micro-Ring Resonator
MWIR	Mid-Wave Infrared
MZM	Mach-Zehnder Modulator
NASA	National Aeronautics and Space Administration
NET	Noise-Equivalent Temperature
NIR	Near Infrared
PD	Photodetector
PDC	Photonic Down-Converter
PIC	Photonic Integrated Circuit
RFI	Radio Frequency Intereference
RIN	Relative Intensity Noise
RMS	Root-Mean Square
SGP	Space Geodesy Project

SLR	Satelitte Laser Ranging
SMA	Sub-Miniature Version A (Connector)
SWaP	Size, Weight, and Power consumption
TNS	Thermal Noise Signal
TRM	Thermo-Reflectance Microscopy
UV	Ultraviolet
VGOS	VLBI Global Observing System
VLBI	Very Long Baseline Interferometry
VNA	Vector Network Analyzer
YBCO	Ytrrium Barium Copper Oxide

Chapter 1: Introduction

"Knowing the spectrum of blackbody radiation, astronomers a century ago correctly deduced that stars having nearly blackbody spectra would be undetectably faint as radio sources, and incorrectly assumed that there would be no other celestial radio sources. Consequently they failed to develop radio astronomy until a strong radio emission from our Galaxy was discovered accidentally in 1932 and followed up by radio engineers." - James J. Condon.

1.1 Brief History of Microwave Radiometers

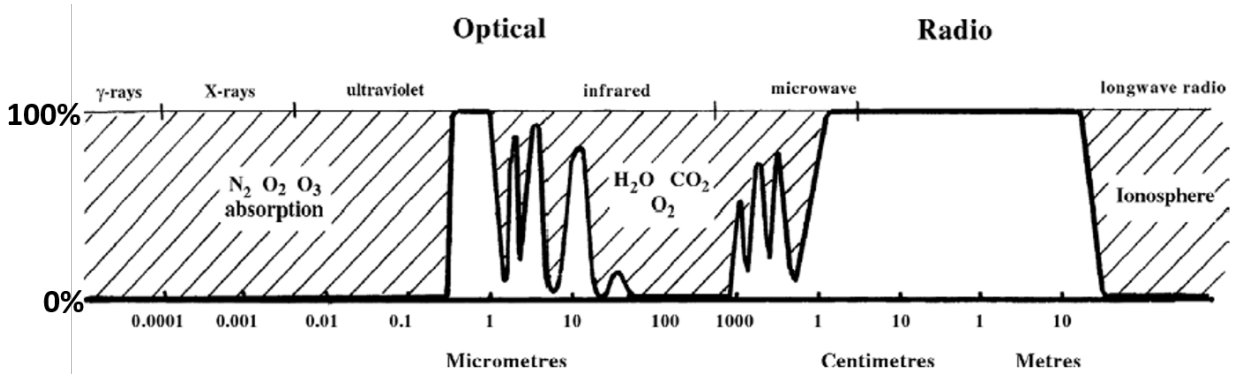

Figure 1.1: Wavelength-dependent transparency of the sky showing several *windows* of opportunity in the optical and radio regions of the electro-magnetic spectrum [1]

A radiometer is an instrument that measures the noise equivalent power of electromagnetic radiation received from the surrounding environment. The Earth's atmosphere absorbs electromagnetic radiation at most infrared (IR), ultraviolet, X-ray, and gamma-ray wavelengths,

but optical/near-IR and microwave wavelength observations of the sky can be made from the ground [3]. Karl Jansky, a radio engineer working for Bell Telephone Laboratories, built an antenna to identify the source of radio interference at 20.5 MHz ($\lambda \approx 14.6$ m). He published his results in 1933, concluding that the noise originated from outside the solar system [6]. Testing several different frequencies with his personal 10 m antenna and receiver in 1939, Grote Reber successfully detected "non-thermal" radiation along the plane of the Milky Way and Andromeda Galaxy at 160 MHz ($\lambda \approx 1.87$ m) [7]. Since its inception, the field of Radio Astronomy has boomed with discoveries of quasars [8], pulsars and neutron stars [9], thermal spectral-line emissions from cold interstellar gas [10], cosmic microwave background radiation from the big bang [11], and many other high-impact astronomical discoveries [3]. Radio sources continue to be discovered to this day, some of which have yet to be fully explained such as Fast Radio Bursts (FRBs) [12].

Microwave radiometers have also found application in the areas of remote sensing and weather forecasting by measuring emitted and reflected radiation from various material surfaces. Microwaves can penetrate clouds and vegetation at certain wavelengths and do not rely on the sun for a source of illumination. Although some microwave wavelengths are attenuated by clouds and rain, this effect can be exploited to gain key geophysical information such as total liquid water fraction, cloud droplet size distribution, atmospheric temperature, and rain intensity [2]. In 1958, a research group at the University of Texas pointed their radiometer antenna down-ward from an elevated vantage point and recorded several radiometric observations at various aspect angles of materials such as water, wood, grass, and asphalt [13]. This field has since evolved into spaceborne platforms. In 1962, the Mariner 2 spacecraft observed Venus with a two-channel radiometer operating at 16 and 22 GHz ($\lambda \approx 1.9$ and 1.35 cm respectively) to measure its hot

surface temperature and relatively cool cloud temperatures [14]. Six years later, Cosmos 243 provided the first radiometric observations of Earth from orbit of sea temperature and salinity at 3.5, 8.8, 22.2, and 37.5 GHz ($\lambda \approx 8.5$, 3.4, 1.35, 0.8 cm respectively) [15]. Nimbus 5 included a microwave spectrometer to measure tropospheric temperature profiles at 22.2, 31.4, 53.7, 54.9, and 58.8 GHz ($\lambda \approx 1.35$, 0.95, 0.56, 0.55, and 0.51 cm respectively). It also housed the Electrically Scanning Microwave Radiometer to derive the liquid and water content of clouds, observe sea ice, and measure soil moisture [16].

Multiple airborne and spaceborne missions are active to this day at even higher frequencies. NASA's Conical Scanning Millimeter-wave Imaging Radiometer (CoSMIR) is in active use for airborne missions on and houses a 9-channel radiometer at 50.3, 52.6, 89 (H & V-pol), 165.5 (H & V-pol), 183.3±1, 183.3±3, and 183.3±7 GHz ($\lambda \approx 0.60$ to 0.16 cm). CoSMIR has been used to estimate snowfall rates, water vapor profiles, light precipitation, and shallow snow cover on the ground [17]. The fields of radio astronomy and microwave remote sensing continue to grow with emerging technologies, radiometer architectures, and measurement techniques.

1.2 Motivation

The main objective of this body of work is to advance various capabilities of radiometers through select instrument technology development efforts which address present and future needs. Interpreting radiometric measurements requires *a priori* knowledge about the measured target. If the instrument is band-limited with fixed observation channels, improving data interpretation could be limited to advancing retrieval algorithms [18]. Ideally, the next generation radiometer is a wideband instrument with improved signal processing capability and lower

size, weight, and power consumption (SWaP) to ultimately provide more data points to compare against scientific models. One challenge with wideband radiometers is impedance matching of components over a wide bandwidth relative to the center operating frequency. It is impossible to create a matching network over all frequencies that matches a pure resistance to an impedance with some reactance [19]. Additionally, a wideband radiometer could be susceptible to man-made signals around certain bands.

Radio Frequency Inteference (RFI) poses one of the greatest challenges to radio astronomy and remote sensing [20]. Out-of-band noise and unwanted man-made signals can lead to narrower observation bands or risk inaccurate measurements. Technical approaches to RFI mitigation include introducing hardware early in the receiver-chain to reject unwanted signals or removing signals in data post-processing [21]. Photonic Integrated Circuits (PIC) intrinsically have a wide absolute bandwidth because the optical carrier frequency is high (193.4 THz for 1550 nm wavelength). Electronic components operating from 1 to 100 GHz require impedance matching over a multidecadal change in frequency. A key process in microwave photonics is to modulate an optical carrier with a spectrum of microwave signals. Impedance matching in the optical region is simplified; an optical signal with a frequency that deviates by up to 100 GHz from the optical carrier may represent less than a .05% change in frequency. PICs also offer opportunities for managing a dynamic environment through tunable filtering, which could pave the way for wideband receivers with flexible measurement capabilities [22]. A programmable photonics-enabled radiometer could prove beneficial for mitigating RFI and detecting unanticipated signals of interest. Millimeter wavelength to THz spectroscopy [23] benefits from the wide absolute bandwidth of electronic components at these wavelengths, but processing the vast spectral content continues to be a challenge for digital spectrometers. PICs may prove instrumental

in aiding digital spectrometers to process the broad spectral content at the required spectral resolutions [24] [25]. Although the SWaP requirements for ground-based instruments may not be as restrictive, spaceborne instruments will face strict SWaP requirements. Electronic hardware needs to survive and operate under intense thermal fluctuations, vibration, and radiation [26] [27]. Measuring instrument components in simulated environments can lead to producing more robust, environmentally-tolerant, radiation-hardened designs [28].

1.3 Organization of Thesis

This thesis explores three published topics to advance the state of the art of radiometer technology. Chapter 2 covers select items in radiation and radiometer theory to clarify the significance of these results. In Chapter 3, a superconducting notch filter with a high-rejection stop-band is developed to mitigate a local, high-power RFI source. Chapter 4 provides a novel photonics-enabled radiometer model to more accurately predict its dynamic range. This chapter also explores the trade-offs between its dynamic range and achievable sensitivity. Thermoreflectance microscopy has been previously demonstrated on PIC components to produce thermal images with sub-micron spatial resolutions [29]. This provides a beneficial technique for testing and subsequently producing robust PIC designs for photonics-enabled radiometers operating in a space environment. Chapter 5 explores the application of thermoreflectance microscopy to a polymer-based photonic interconnect known as Photonic Wire Bond (PWB). PWB enables the coupling of multiple PIC devices without requiring active optical alignment.

There are often changes in variable symbols to represent equivalent physical parameters. For example, radio frequency is represented by ν in Chapter 2 while discussing radiation and

radiometer theory, as ω when discussing microwave filter design in Chapter 3, and as Ω when discussing microwave photonics (to distinguish it from the optical carrier frequency). Instead of pursuing uniformity, these variable symbols are clearly defined in each chapter and left intact to be consistent with the most common usage elsewhere in literature for the subject matter.

Chapter 2: Relevant Theory

This chapter presents a brief selection of established theory that is useful for understanding the nature and impact of the topics explored in this thesis. There are different sources of detectable radiation important to radio astronomy and different factors to consider for remote sensing that are not covered here. What is important for understanding subsequent chapters is knowing what a radiometer is measuring, how the measurement can vary as a function of frequency, and that RFI, non-linearities, and instrument-generated power-fluctuations can impact measurement accuracy. For a more complete background on microwave radiometry and remote sensing, I recommend reviewing "Essential Radio Astronomy" by James J. Condon and Scott M. Ransom [3], as well as "Microwave Radar and Radiometric Remote Sensing" by David Gardner Long and Fawwaz T. Ulaby [2].

2.1 Radiation Fundamentals

Consider a source of radiation where the distance of the source from the observer is much greater than its size. This is known as a *point-source*. Using the ray-optics approximation, we can assume that radiation emitted by this source is propagating in a straight line, perpendicular to a wave-front [3]. The specific intensity or spectral brightness of this radiation is defined as:

$$I_\nu = \frac{dP}{A\, d\Omega\, d\nu} \tag{2.1}$$

where dP is the power received by a detector with a projected surface area A and solid angle $d\Omega$ measured from the observer's location. This chapter will maintain use of frequency (ν) for units because the focus is in the microwave domain. However, a simple substitution of $\nu = c/\lambda$ will convert any equation presented here to its wavelength-dependent description, which may feel more appropriate for readers more familiar with the optical domain. In literature, B_ν may be used to refer to the specific intensity at the source whereas I_ν refers to the specific intensity along the ray path. These values will likely be different due to absorption or emission along the ray path, scattering or diffraction at the antenna, or other cosmological effects [1]. Here, only I_ν is used.

In 1914, Max Planck published "The Theory of Heat Radiation", which describes the spectrum of electromagnetic radiation emitted by a black-body at a given temperature [30].

$$I_\nu = \frac{2h\nu^3}{c^2} \frac{1}{\exp\left(\frac{h\nu}{k_B T}\right) - 1} \tag{2.2}$$

where h is Planck's constant and k_B is Boltzmann's constant. A blackbody is an ideal physical body, consisting of a uniform medium in thermal equilibrium at temperature T, that absorbs and emits incident electromagnetic radiation at all frequencies. Most sources are not true blackbodies, instead referred to as a "grey body". That is, they are not perfect absorbers and emitters of radiation. Instead, they may reflect light at some frequencies and will not emit light

with perfect efficiency.

Figure 2.1 shows multiple traces of Equation 2.2 plotted with the different parts of the electromagnetic spectrum identified. It is apparent from this figure that at lower frequencies, specific intensity has a quadratic dependence on frequency. In the microwave region of the electromagnetic spectrum where $h\nu \ll k_B T$, the simplified Rayleigh-Jeans approximation for specific intensity can be used [31]:

$$I_\nu = \frac{2k_B T \nu^2}{c^2} \tag{2.3}$$

Depending on the context in future usage, T may be understood either as the physical temperature of a blackbody source or an equivalent *brightness temperature*. In the Rayleigh-Jeans approximation, the brightness temperature of a source is the temperature a blackbody would have to be to fit the observed grey body source.

Adjustments would need to be made when making observations in the milimeter-wave to sub-milimeter-wave regions of the spectrum [23]. Equation 2.2 can be rewritten in term of power spectral density:

$$P_{\mathrm{bb},\nu} = h\nu \frac{1}{\exp\left(\frac{hv}{k_B T}\right) - 1} \tag{2.4}$$

As well as the Rayleigh-Jean approximation for lower frequencies:

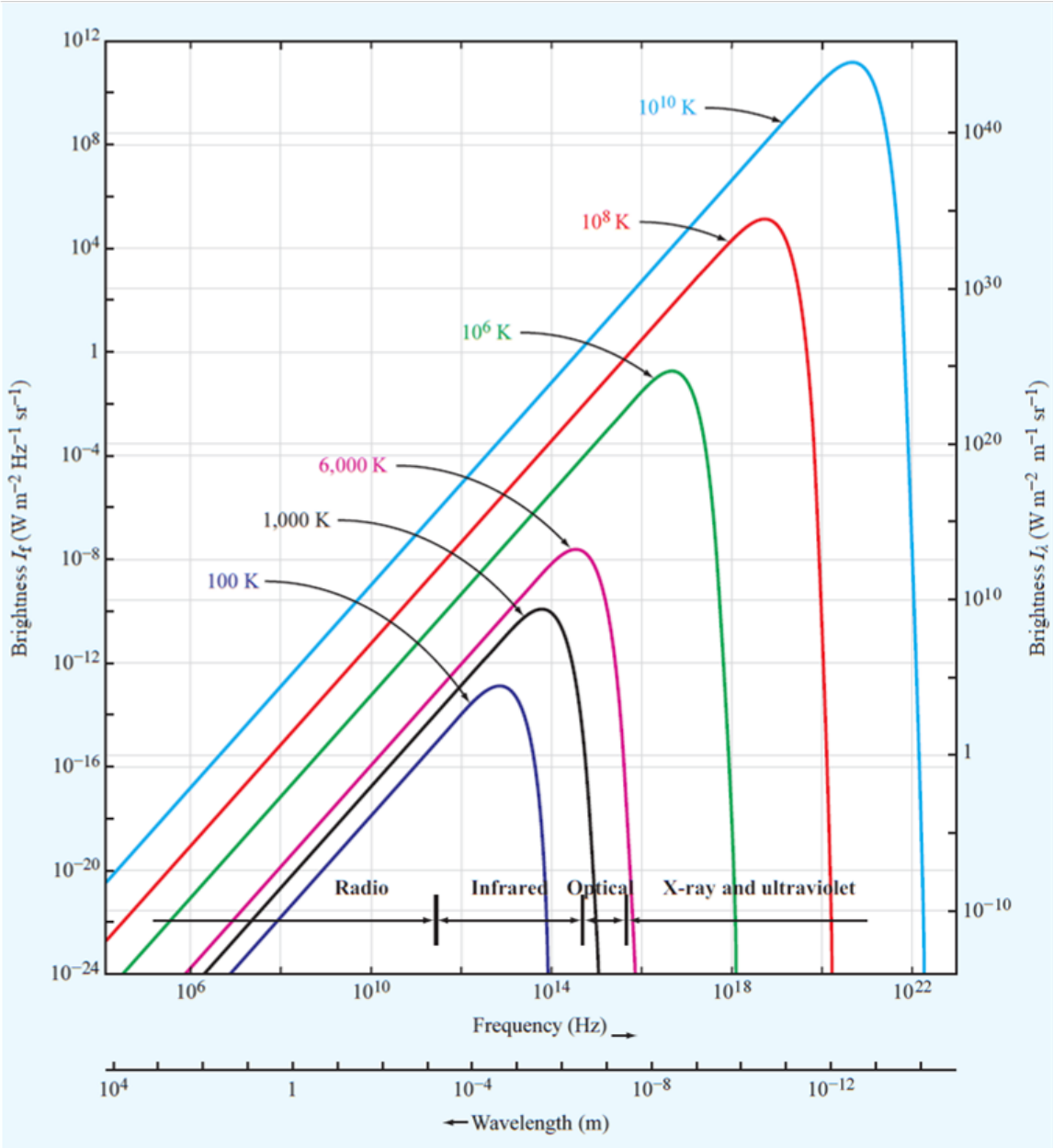

Figure 2.1: Traces from Planck's radiation law plotted at different temperatures [2]

$$P_{\mathrm{bb},\nu} = k_B T \tag{2.5}$$

In 1928, John Johnson and Harry Nyquist at Bell Laboratories found that the thermal noise

generated in a resistor with resistance R, has the same root-mean-square voltage that is proportional to the temperature of the resistor (T) and the measured bandwidth ($\Delta\nu$) [32]:

$$v^2_{\mathrm{n,rms}} = 4Rk_BT\Delta\nu \tag{2.6}$$

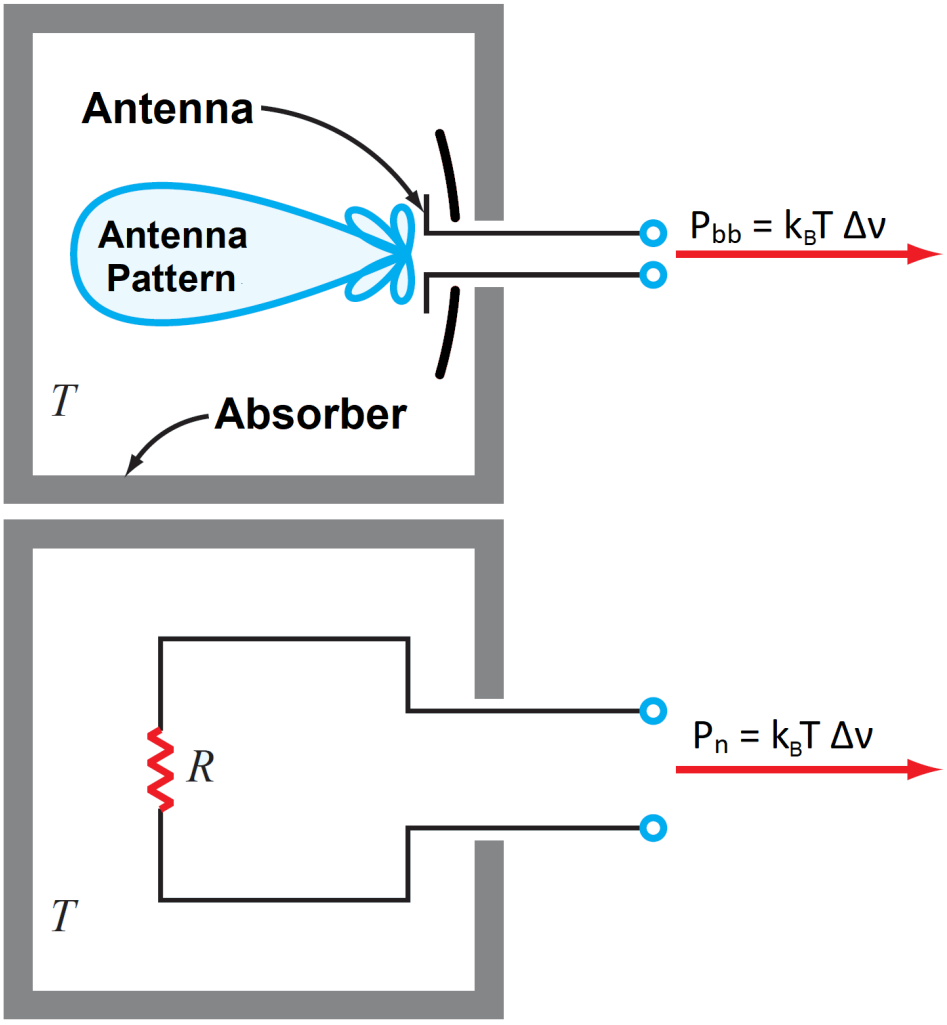

Figure 2.2: The noise generated in an impedance-matched resistor will generate an equivalent amount of noise power as an antenna measuring the surrounding blackbody radiation if each are enclosed in an appropriate absorber and held at an equivalent temperature.

Figure 2.2 illustrates two scenarios, one in which the antenna of a receiver is enclosed in a temperature-controlled absorber and another where the antenna is substituted with a resistor. In both cases, the measured noise power integrated over bandwidth $\Delta\nu$ is

$$P_{\mathrm{bb}} = P_{\mathrm{n}} = k_B T \Delta\nu \tag{2.7}$$

This information is useful for instrument calibration. As discussed later in Section 2.3, it will turn out that both the measured signal and internally-generated noise in the instrument follow similar stochastic processes and are typically indistinguishable. However, a temperature-controlled, impedance-matched load may be used to calibrate the instrument to a known temperature. The radiometer should have a linear power response. If electronics are saturated due to RFI, or if the device is deliberately tuned so changes in input power exhibit a non-linear response, then a measured change in power will not correspond linearly to a change in observed brightness temperature.

2.2 Radiative Transfer and Spectral Lines

Now consider radiation propagating along a ray that passes through some medium before reaching the detector as depicted in Figure 2.3. The intensity of the radiation will change according to added emissions and absorption in the medium. This is described by:

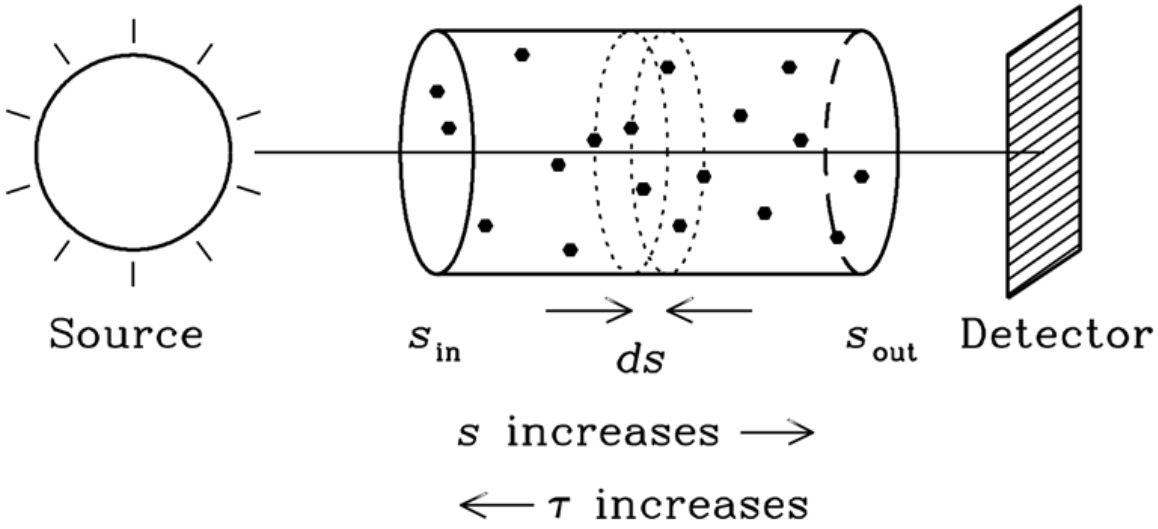

Figure 2.3: Radiation passes through a medium along a ray where there may be an impact to its intensity due to absorption and emissions in the medium [3]

.

$$j_\nu \equiv \frac{dI_\nu}{ds} \tag{2.8}$$

$$\kappa_\nu \equiv \frac{dP(\nu)}{ds} \tag{2.9}$$

$$\frac{dI_\nu}{ds} = j_\nu - \kappa_\nu I_\nu \tag{2.10}$$

where j_ν is the emission coefficient for the increase in specific intensity per unit distance through the medium. κ_ν is the linear absorption coefficient, which is the probability ($P(\nu)$) that a photon will be absorbed in a medium layer of thickness ds. Another useful definition is *optical depth*, where the absorption is integrated along the length (l) of the medium along the direction of propagation:

$$\tau_\nu(s) \equiv \int_0^l \kappa_\nu(s')\, ds' \tag{2.11}$$

As long as this medium is uniform and can be described by a single temperature, such that it is in local thermodyanmic equilibrium, Kirchoff's radiation law states that the emitted radiation must be equal to the absorbed radiation [33]:

$$I_\nu(T) = \frac{j_\nu}{\kappa_\nu} \tag{2.12}$$

The specific intensity in Equation 2.8 can be described in terms of optical depth:

$$I_\nu = I_\nu^0 e^{-\tau_\nu} + S_\nu(1 - e^{-\tau_\nu}) \tag{2.13}$$

Where I_ν^0 is the initial specific intensity incident on the medium. The source function S_ν shares the same units as the specific intensity and is a measure of how much energy from the original source is removed from the path and replaced by energy generated in the medium [1]. Since the specific intensity, absorption, and emission are frequency-dependent; the measured intensity will also be frequency-dependent. A meaningful example of how this is useful is a zenith sky-observation made across the electromagnetic spectrum from the ground. Figure 1.1 shows *windows* can be identified at different bands. Using the Rayleigh-Jeans approximation at the appropriate wavelengths, the specific intensity can also be described by the brightness

temperature.

$$T_{\mathrm{A}} = T_{\mathrm{source}} e^{-\tau_\nu} + T_{\mathrm{medium}}(1 - e^{-\tau_\nu}) \tag{2.14}$$

Where T_A is the equivalent temperature of radiation measured at the antenna, which will likely vary with frequency in practice due to the process described above.

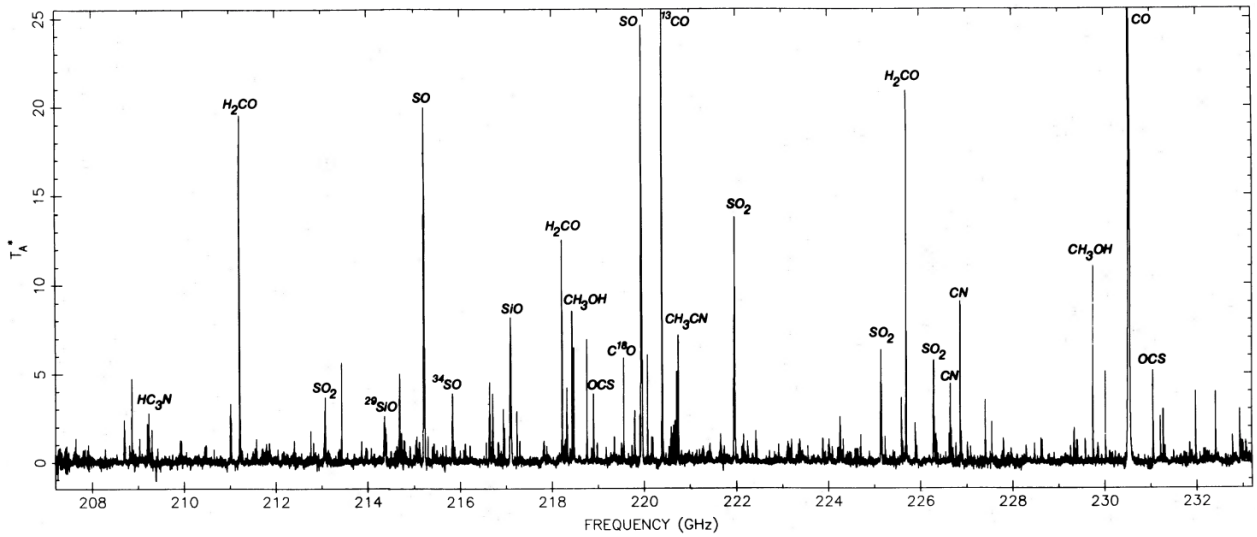

Figure 2.4: Compressed view of the Caltech Owens Valley Radio Observatory (OVRO) millimeter-wave spectral line survey of Orion molecular cloud (OMC-1) [4]

Across the spectrum, there could also be many emission or absorption features as seen in the example in Figure 2.4. These spectral features have linewidths as narrow as sub-Hz and are the result of a variety of quantum mechanical processes that are described elsewhere, such as vibrations and rotational transitions of molecular species which comprise the cloud [1]. If a wideband spectrum can be processed in narrow-band parts, molecular species can be resolved identified. As mentioned in Chapter 1, there may also be spectral content apparent from man-

made sources radio frequency interference (RFI). Unwanted RFI could be removed from select bands to improve measurement accuracy of the neighboring signals of interest. The following section describes the basic operation of a radiometer and the different configurations available to measure the brightness temperature of these sources.

2.3 Radiometers

Radiometers could be considered as thermometers for distant blackbody sources. These instruments measure the brightness temperature of distant sources in the microwave to far-infrared region of the electromagnetic spectrum. The typical radio emissions of interest here are randomly generated by natural processes, such that the measured noise voltage has a Gaussian amplitude distribution around a zero mean value. A square-law detector will square the input noise voltage and produce an output voltage signal that is proportional the input noise power. The measured source signal should be *stationary* or steady on a long timescales compared with the inverse frequency to obtain an acceptable average. A radiometer detector could directly rectify and measure the integrated power of the signal over its bandwidth in a *direct detect* configuration. It could also down-convert the signal's carrier frequency to a lower frequency to allow for digitally sampling and resolving the spectrum. This configuration is known as a *superheterodyne* (or more generally as "heterodyne") radiometer. According to the Nyquist-Shannon sampling theorem, the detector should be sampled at a rate faster than $(2\Delta\nu)$ where $\Delta\nu$ is the detector bandwidth [34]. In a *spectrometer*, the radiometer bandwidth can also be divided into multiple channels with unique frequency boundaries and down-converted to a lower carrier frequency. This reduces the sampling rate required to process the full instrument bandwidth. In any case, the amplified noise

internally generated by the radiometer is likely much larger than measured noise power from the source. In order to measure small changes in power, the measurement will be averaged over a large number of independent samples $N = (2\Delta\nu\tau)$ where τ is the duration of sampling or *integration time*.

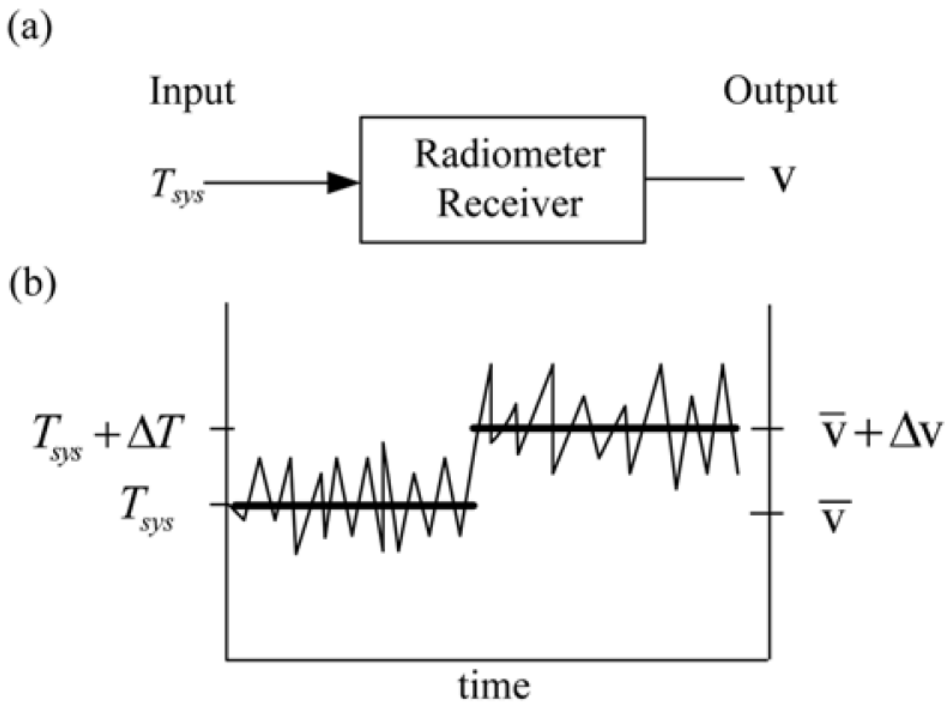

Figure 2.5: (a) block diagram and (b) corresponding plot showing how a small change in input temperature can be detected by averaging over a large number of samples [5]

Figure 2.5 illustrates how a small change in temperature can be detected over a large number of samples. T_{sys} represents the noise equivalent temperature of the radiometer and incorporates the total noise contributions generated from internal components. When a signal is introduced, the small change in brightness temperature ΔT is measured as Δv. The smallest achievable ΔT is known as the *radiometric resolution* for a radiometer and is described by the ideal radiometer equation:

$$\Delta T \approx T_{sys} \frac{1}{\sqrt{\Delta \nu \tau}} \tag{2.15}$$

A larger bandwidth will improve radiometric resolution, but could introduce error due to RFI. It could also limit processing of narrow spectral lines. A longer integration time will also improve the radiometric resolution. In reality, there are often periodic gain fluctuations at longer time scales (seconds) that could be caused by multiple sources, such as $1/f$ noise attributed to semiconductors [35]. This is a more generalized form for the radiometer equation:

$$\Delta T \approx T_{sys} \sqrt{\frac{1}{\Delta \nu \tau} + \left(\frac{\Delta G}{G}\right)^2} \tag{2.16}$$

Where $\Delta G/G$ represents the normalized gain fluctuations in the radiometer. This means there will be an optimal integration time to minimize radiometric resolution. The integration time could be further limited depending on the application, such as if the radiometer has a narrow observation window of the target. These limits will also determine when a calibration should be performed.

2.4 Calibration

In order to distinguish the radiometer noise equivalent temperature and gain fluctuations from the source signal, the instrument needs to be periodically calibrated. The power response of the radiometer should be linear. Otherwise a more complex, multi-point calibration scheme

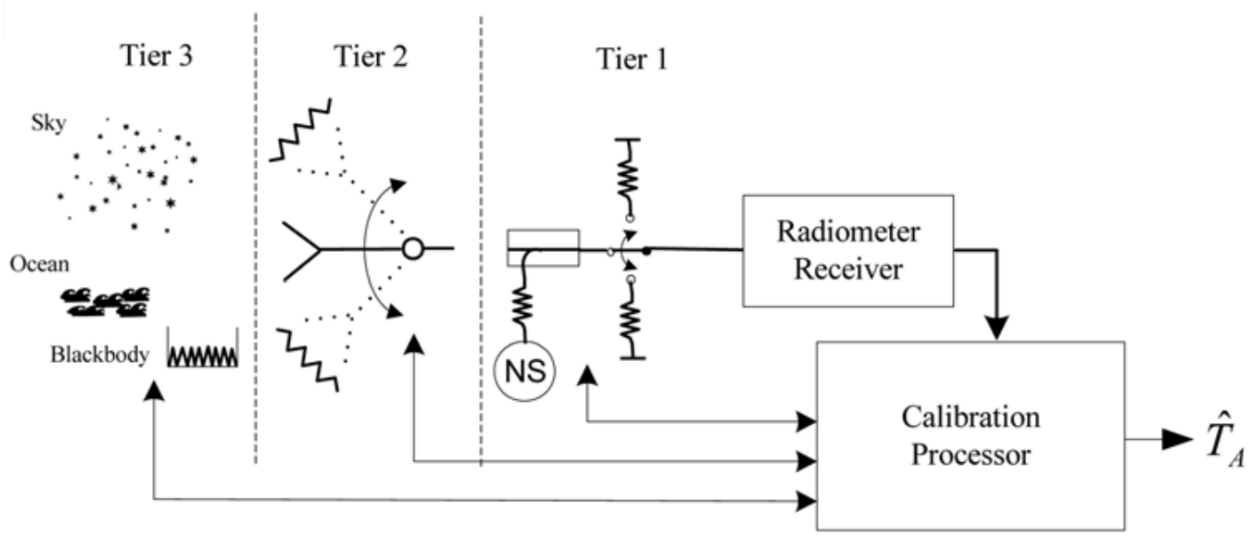

Figure 2.6: Generic model for radiometer calibration architecture illustrating three tiers of calibration. Tier 3 comprises calibration references external to the radiometer. Tier 2 includes internal calibration references that are observed through the antenna. Tier 1 includes references or noise sources integrated directly into the radiometer. [5]

may be required. A typical two-point linear calibration can be achieved by measuring the noise power of two references controlled to known temperatures, one hot (subscript H) and the other cold (subscript C) relative to each other. The radiometer detector will measure these powers:

$$P_{\mathrm{H}} = Gk(T_{\mathrm{sys}} + T_{\mathrm{H}})\Delta\nu \tag{2.17}$$

$$P_{\mathrm{C}} = Gk(T_{\mathrm{sys}} + T_{\mathrm{C}})\Delta\nu \tag{2.18}$$

The ratio between these measurements is the *Y-factor* and the receiver's equivalent temperature can be determined as follows:

$$Y \equiv \frac{P_{\mathrm{H}}}{P_{\mathrm{C}}} = \frac{T_{\mathrm{sys}} + T_{\mathrm{H}}}{T_{\mathrm{sys}} + T_{\mathrm{C}}} \tag{2.19}$$

$$T_{\mathrm{sys}} = \frac{T_{\mathrm{H}} - Y T_{\mathrm{C}}}{Y - 1} \tag{2.20}$$

There are multiple tiers of calibration possible as depicted in Figure 2.6. One option, the celestial method, is to measure known external references (tier 3). This requires orientation towards multiple targets. Integrating a calibration target into the system allows the temperature to be controlled and incorporates the noise equivalent temperature of the antenna into the calibration measurement (tier 2). In situations where it is impractical to integrate a calibration target into the system, temperature-controlled resistors can be used in place of the antenna (tier 1). The antenna and thermal load should have a good impedance match with the radiometer. Introducing a noise source, commonly consisting of a back-biased Zener diode, will increase the injected noise power and may make it easier to perform calibration measurements more frequently [1]. The noise is injected through a coupler where the noise source is toggled on and off. In a *Dicke Switched Radiometer*, the receiver is rapidly switched between the alternate signal paths to the antenna and reference load [36]. The waveform used to drive the switch also drives a lock-in amplifier. This switched radiometer minimizes the impact of gain variations between signal measurement and reference. If the system is balanced such that $T_{\mathrm{ref}} = T_{\mathrm{sys}}$, then T_{sys} is automatically subtracted out. Two consequences of this method are 1) a switch placed before a low-noise amplifier (LNA) will increase losses and degrade sensitivity and 2) the radiometric resolution is effectively doubled because the antenna temperature and reference load are measured for only half of the time.

Chapter 3: Superconducting Notch Filter

This section is based on work from the following publication: C. J. Turner, T. Stevenson, R. Cantor, L. Hilliard, T. E. Murphy and B. Bulcha, "Superconducting Notch Filter for RFI Mitigation in Ground-Based Radio Telescope," in IEEE Transactions on Applied Superconductivity, vol. 33, no. 3, pp. 1-5, April 2023, doi: 10.1109/TASC.2023.3243492.

3.1 Overview

Radio Frequency Interference (RFI) mitigation can have a critical impact on the performance of radiometers used for radio astronomy. RFI consists of any undesired, in-band or out-of-band, man-made signals or naturally generated noise emissions detected by the receiver. The presence of RFI signals can increase the detected power and estimated antenna temperature, or even saturate active electronic components, leading to inaccurate measurements [37]. In ground-based radio astronomy, cryogenic receivers can provide the necessary sensitivity to detect especially weak RF-signals, but are especially susceptible to local RFI [38] [39].

Superconducting microwave filters consist of conductors that have electrical resistance to direct current below a known transition temperature. As a result, these filters can be placed between the aperture and low-noise amplifier in a cryogenic receiver to reject RFI with a minimal impact to the receiver's sensitivity. This chapter covers the design, fabrication, and measurement

of a thin-film, high-temperature superconductor (HTS) notch filter to address the RFI mitigation needs of a radio telescope located at the Goddard Geophysical Astronomical Observatory (GGAO) in Greenbelt, MD. The filter operates at 2-12 GHz and its rejection bandwidth, centered on 9.4 GHz, currently demonstrates the highest reported fractional bandwidth, 4.3%, for 50 dB of signal rejection. The frequency response of this filter also exhibits an excellent square-like notch profile; the fractional bandwidth for 20 dB of signal rejection is less than or comparable to many previously reported HTS notch filters with relatively worse rejection performance.

The key concern with this effort is achieving a band-stop rejection not previously demonstrated in literature for microstrip HTS filters. First, this chapter presents the challenge at GGAO and provides a brief description of previous efforts toward RFI mitigation for ground-based radio receivers in Section 3.2.1. Additionally, it summarizes prior work in superconducting microwave filters with an emphasis on components fabricated with HTS materials in Section 3.2.2. Section 3.3 describes reasoning behind selecting thin-film Yttrium Barium Copper Oxide (YBCO) conductor on sapphire (Al_2O_3) substrate for this filter design and the impact of these material properties on the design process. Sections 3.4 and 3.5 cover the process of circuit design, simulation and selection of the resonator topology, and the physical layout of the filter. In Section 3.5, simulation results are presented for a 3D electromagnetic (EM) model, providing a higher-fidelity filter response and accounting for the impact of fabrication tolerances. Finally, this chapter provides a summary of the filter measurements and a comparison to previous HTS filter designs in Section 3.6, and concludes with a discussion on the importance of these results for RFI mitigation Section 3.7.

Figure 3.1: Photo of the 12 m GGAO VGOS antenna (courtesy of NASA SGP)

3.2 Background

3.2.1 Ground-based Radio Astronomy and RFI Mitigation

The receivers in radio telescopes detect and measure broadband radio emissions from celestial sources. Typically, these emissions are measured at low power levels (10^{-15} to 10^{-20} Watts) and consist of incoherent radiation with statistical properties that are indistinguishable from the noise generated in the receiver or emitted by sources of background radiation [40]. Contributors to RFI can include emissions from wireless communications, navigation systems, or radar and these sources often limit the sensitivity of radio astronomical stations. Choosing the optimal RFI mitigation technique depends on the type of radio telescope (single dish or connected interferometer), the type of observations (continuum or spectral), and the type of RFI (impulse-like bursts,

narrow-band, or wideband [41]. Technical approaches to RFI mitigation may take place at the system-level, in the RF front-end, the digital back-end, or in post-processing of the data [21]. According to the International Telecommunication Union (ITU) Report ITU-R RA.2126-1, a summary of RFI mitigation techniques include *pro-active measures* to change the local RFI environment through careful planning and choosing the observatory's location, *spatial nulling* or adaptive spatial filtering by using array beam-forming techniques to orient pattern nulls toward the RFI source, *waveform subtraction* where the RFI signal is directly removed from the data through a model or reference signal, *anti-coincidence* where RFI is discriminates from the signal with widely-separated antennas that measure the same signal and different background noise, and *excision in the temporal or frequency domain* where the RFI is removed from the measurement or the data.

The filter presented in this chapter falls under the *excision in the frequency domain* RFI mitigation technique and its design requirements specifically address the needs of a radio telescope at the Goddard Geophysical Astronomical Observatory (GGAO). Very Long Baseline Interferometry (VLBI) is a high angular resolution geodetic technique that uses cosmic radio sources as a reference to accurately measure global reference frames and monitor Earth's orientation and variations. VLBI Global Observing System (VGOS) is the next-generation network of 12 m telescopes that provide broadband receiver systems with four frequency bands ranging from 2 to 14 GHz and high data rates to achieve a measurement accuracy of 1 mm in station position and 0.1 mm/year in station velocity on global scales [39, 42]. GGAO is home to one of these VGOS helium-cooled receivers in Greenbelt, MD. Co-located approximately 110 m from this receiver, the Satellite Laser Ranging (SLR) system uses a 9.4 GHz radar to detect and prevent accidental illumination of overhead aircraft [43]. Under certain orientations, the VLBI receiver will mea-

sure one of the radar's sidelobes. This scenario will saturate the front-end LNA and compromise receiver sensitivity, as well as potentially damage sensitive electronics [44]. The presence of this interfering source imposes constraints on the dish orientation, sky coverage, and schedule; limiting both the scope and duration of observations.

3.2.2 Superconducting Microwave Filters

Fortunately, the RFI carrier frequency impacting the VGOS receiver at GGAO falls between its various observation bands and a suitable, low loss, stop-band (i.e. "notch") filter prior to the low-noise amplifier (LNA) would both protect sensitive electronics and enable uninterrupted full-sky observation. Superconductors are materials that can be characterized with zero electrical resistance (among other effects) when cooled below its transition temperature (T_c and the HTS term refers to superconductors with higher transition temperatures resulting from the discovery of ceramic cuprates [45]. It is practical to consider HTS as having a T_c higher than the boiling point of liquid nitrogen (77 K), although not all categorized HTS meet this criteria. HTS filters have been employed in radio astronomy receivers in the past [46]. However, thin-film HTS notch filter designs are not as widely studied as their band-pass counterparts. Other resonator geometries have been measured at high external quality-factors, but impose an increased risk to the device performance for this application due to the potential for high current densities localized near their small features (such as interdigital fingers or narrow meander lines) [47–52]. HTS bulk disk and patch resonators have demonstrated higher power-handling capabilities [53–55], but in practice these bulkier resonators would not allow us to simultaneously achieve the necessary bandwidth (bounded by 50 dB of rejection) and volume requirements. Although not essential for

this application, this filter layout is compatible with and could be modified by other filter design techniques such as Defected Ground Structure (DGS) [56] and cul-de-sac coupling configuration [57] to tailor its performance to other requirements.

For the filter presented in this chapter, HTS planar circuits are used to minimize insertion loss in the pass-band and meet a strict form factor of 25 mm width, 32 mm length, and 6 mm height to fit in available space inside the existing receiver dewar. This notch filter must handle the higher-power radar sidelobe without a change in performance and requires at least 50 dB of signal rejection over 250 MHz of bandwidth with the stop-band centered on 9.4 GHz. To the best knowledge of the author, no prior published HTS planar notch filter design has demonstrated a 50 dB fractional bandwidth of 2.7% in measurement. The filter design consists of seven modified hairpin resonators where the arms are folded to increase parallel coupling. The self-coupled hairpin resonator geometry provides the necessary shunt reactance to achieve higher stop-band rejection, demonstrates good quality factors to avoid significantly increasing insertion loss in the observation bands, and avoids the use of narrow-width microstrip or interdigital features. Current concentration at the resonator edges are the limiting factor in power handling capacity of HTS filters [58]. Using small features as in some other designs [59, 60] increases the amount of fringing electric fields along the microstrip edges and risks degrading the filter's performance while exposed to the local, high-power RFI source.

3.3 Materials Selection

The physics behind and application of HTS for microwave electronic devices has been extensively discussed in literature [61]. Multiple HTS materials have been previously investigated,

including EBaCuO ($T_c \approx 92$ K [62]), GdBaCuO ($T_c \approx 92$ K [63]), YBaCuO ($T_c \approx 93$ K [64]), BiSrCaCuO ($T_c \approx 110$ K [65]), HgBaCaCuO ($T_c \approx 147$ K [66]), and TIBaCaCuO ($T_c \approx 128$ K [67]). A higher T_c is desirable for relaxing the power cost for cooling the device. If the device is cooled to a lower temperature, such as with liquid helium (4 K), a higher T_c allows for greater signal power handling due to heating [68]. Regardless, YBCO (short-hand for YBaCuO) has had the most commercial success due to the relative ease of the fabrication process. Fabrication of YBCO-based microwave devices has been demonstrated on multiple substrates, the most promising include $LaAlO_3$ [69], MgO [70], $LiNbO_3$ [71], and Al_2O_3 (sapphire) [72] among others. The dielectric constant of $LaAlO_3$ and Y-cut $LiNbO_3$ are approximately 24 and 28 respectively, forcing relatively large microstrip geometries to create impedance-match devices with a standard characteristic impedance of 50 Ω.

The team working on this effort selected 300 nm thin film YBCO on 435 μm thick sapphire substrate from STAR Cryoelectronics. STAR Cryoelectronics is a US company based in New Mexico with a high-quality YBCO-on-sapphire process. One key advantage to sapphire over MgO is the ability to employ larger wafers. The "R-plane" of the crystal was selected to ensure good epitaxial growth of YBCO and results in high-quality films with minimized surface resistivity. Sapphire provides low-dielectric losses and high thermal conductivity, but requires accurate electromagnetic (EM) simulation to address its anisotropic permittivity [73]. The diagonalized permittivity matrix for the sapphire in crystal frame with the c-axis oriented to the z-axis of the film is:

$$\varepsilon_{\mathrm{k}} = \begin{bmatrix} 9.3000 & 0.0000 & 0.0000 \\ 0.0000 & 9.3000 & 0.0000 \\ 0.0000 & 0.0000 & 11.5000 \end{bmatrix}$$

To simplify the design, the circuit was oriented on the wafer such that the diagonal values of the matrix were approximately equal. This is equivalent to a rotation operation and the resulting permittivity matrix used in simulation is:

$$\varepsilon_{\mathrm{r,waffer}} = \begin{bmatrix} 10.0842 & -0.7842 & 0.7038 \\ -0.7842 & 10.0842 & -0.7038 \\ 0.7038 & -0.7038 & 9.9316 \end{bmatrix}$$

The selected substrate thickness and filter layout ensured a wide safety margin between the simulated current density and critical current density of the YBCO, such that the device could reliantly handle a 1 Watt RFI signal with 50 Ω microstrip transmission lines when cooled to 20 K. A 3D EM CAD Model was designed and simulated in Ansys HFSS simulation software. This model contained the anisotropic permittivity matrix and its impact on the design process is discussed in section 3.5.

3.4 Circuit Design

Microwave filter design has a rich history dating back to World War II and has been thoroughly developed in prior literature [74] [75]. Typically, modern microwave filter design is conducted with CAD software based on the insertion loss method. The insertion loss method is a network synthesis technique to design filters with a completely specified frequency response [76]. This method uses network synthesis techniques to product filter circuits with n-elements normalized in impedance and frequency [75]. Through the application of various transformations and identifies, different filter types (low-pass, high-pass, band-pass, band-stop, etc) can be produced by substituting between series and shunt lumped circuit elements or introducing distributed circuit elements while maintaining the desired filter response. In this section, a modification is made to the derivation for a band-stop filter circuit presented in the textbook "Microstrip Filters for RF/Microwave Applications" [77].

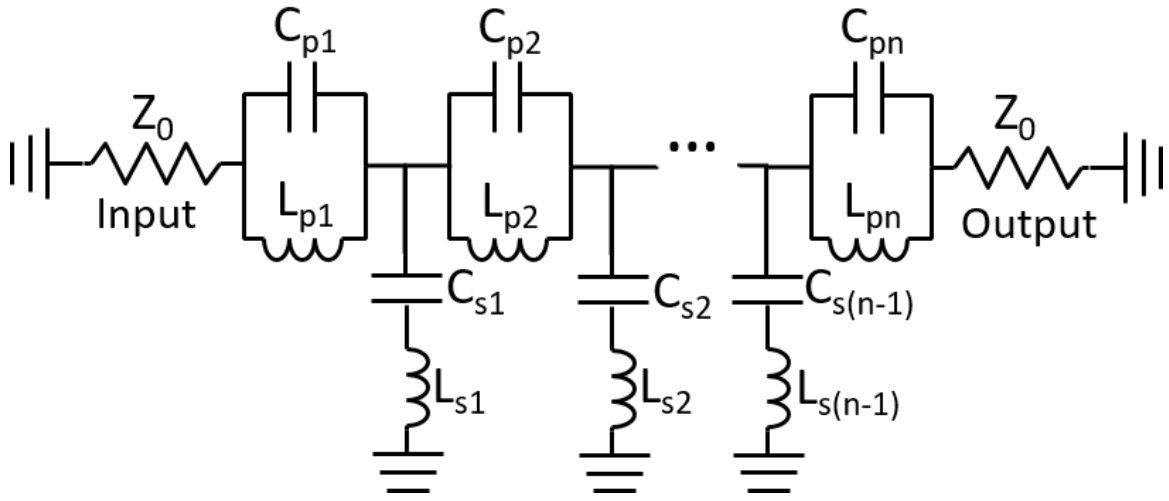

Figure 3.2: Lumped Circuit n-Element Notch Filter
(**p** - series **p**arallel-resonant branch, **s** - shunt **s**eries-resonant branch)

This filter design requires a 50-dB fractional bandwidth greater than 2.7%, and a 3-dB fractional bandwidth less than 5.3% to maximize stop-band RFI signal rejection and minimize pass-band insertion loss. Using a Chebyshev model to achieve the desired filter response, the required reactance slope values and external Q-factor (Q_e) values are as large as 845 Ω and 35, respectively [77]. These relatively large values can be difficult to physically realize with planar microstrip. A typical planar microstrip notch filter design consists of a series of coupled half-wavelength resonators, each positioned a quarter-wavelength apart (with respect to the filter's center frequency ω_0) along the direction of propagation [77]. However, these designs limit coupling between the length (l) of the resonator and transmission line, making it difficult to achieve a larger coupling capacitance. Decreasing the gap between the resonator and the transmission line will increase this capacitance, but only at the expense of decreasing its quality factor. The equivalent lumped-element circuit for a basic band-stop filter is depicted in Figure 3.2.

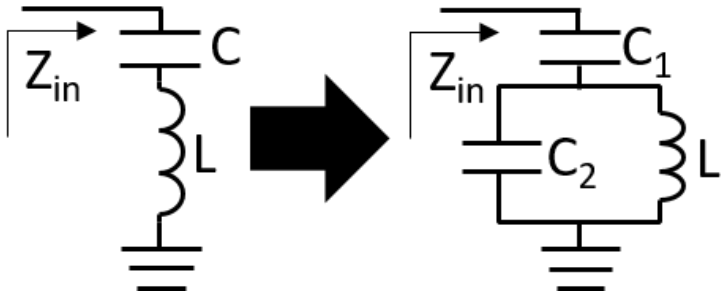

Figure 3.3: (Left) Series LC resonator circuit and (Right) Equivalent lumped circuit model for self-coupled hairpin resonator.

In order to understand how this filter improved on the state-of-the-art in a high-rejection stop-band, it is useful to consider a key design strategy described with a basic lumped element circuit. The ideal circuits depicted in Figure 3.3 are purely reactive. The circuit on the left is a common series LC circuit. A few interesting things happen when this circuit is modified by

adding a capacitance (C_2) in parallel to the inductance (L). These effects will ultimately help improve realization of a high-rejection filter in microstrip. In the following derivations, $C = C_1 + C_2$ is constrained to quantify the impact on adding a parallel capacitance (C_2) to the series LC circuit. The impedance of the circuit illustrated to the right in Figure 3.3 is given by:

$$Z_{\text{in}}(\omega) = \frac{1}{j\omega C_1} + \frac{1}{\frac{1}{jwL} + j\omega C_2} = \frac{1 - \omega^2 L(C_1 + C_2)}{j\omega C_1(1 - \omega^2 L C_2)} \tag{3.1}$$

The circuit in Figure 3.3 will resonate at $\omega = \omega_0$ when $Z_{\text{in}} = 0$. This results in:

$$\omega_0^2 = \frac{1}{L(C_1 + C_2)} \tag{3.2}$$

Notice if C_1 = C and C_2 = 0, then Eq. 3.2 converges to $\omega_0 = \frac{1}{LC}$ as expected for a series LC circuit. The reactance slope is equivalent for both resonator circuits:

$$x = \frac{\omega_0}{2} \left. \frac{\mathrm{d}X(\omega)}{\mathrm{d}\omega} \right|_{\omega=\omega_0} = \left(\frac{C_1}{C_1 + C_2} \right)^{-2} \omega_0 L = \alpha \omega_0 L \tag{3.3}$$

In a multi-element filter design, this resonator may be implemented as a shunt element [77]. In the narrow-band case where $\Delta\omega = |\omega_0 - \omega| \ll \omega_0$, the insertion loss and external quality factor of this resonator is:

$$|S_{21}| \approx \left[1 + \left(\frac{1}{4(x/Z_0)}\frac{\omega_0}{\Delta\omega}\right)^2\right]^{-1/2} \tag{3.4}$$

$$Q_e = \frac{\omega_0}{\Delta\omega_{3\text{dB}}} = \frac{2x}{Z_0} = \alpha\frac{2}{R}\sqrt{\frac{L}{C}} \tag{3.5}$$

In this form, the impact of this parallel capacitance (C_2) on the quality factor and resonant frequency can be quantified as:

$$\omega_0^2 = \frac{1}{LC} = \frac{1}{L(C_1 + C_2)} = \frac{\beta^2}{LC_1} \tag{3.6}$$

where:

$$\alpha = \left(1 - \frac{C_2}{C}\right)^{-2}, \beta = \sqrt{1 - \frac{C_2}{C}} \tag{3.7}$$

When the reactance slope, quality factor, and resonant frequency are presented in this form, it is helpful to see the impact of increasing the parallel capacitance (C_2) while R, L and $C = C_1 + C_2$ are held constant. As C_2 increases, C_1 decreases such that the ω_0 remains constant. Fig. 3.3 illustrates the change in α and β as C_2/C is increased. The reactance slope (x) and quality factor (Q_e) are proportional to α and increasing the reactance slope will increase the signal rejection at frequencies close to ω_0. As a result, increasing C_2 reduces the required coupling capacitance (C_1) and enables its use in narrow-band filter designs. An additional advantage is

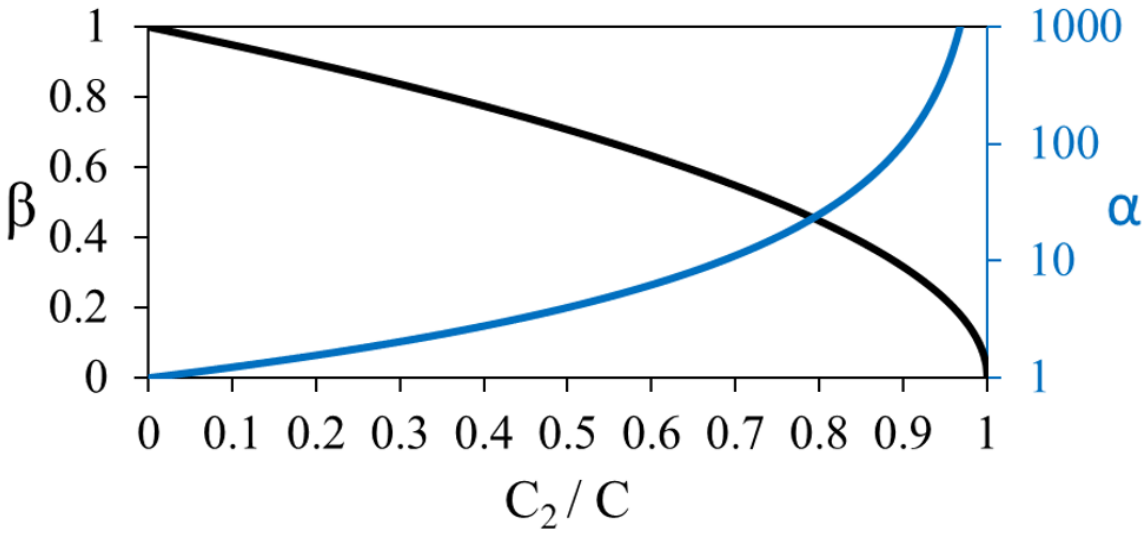

Figure 3.4: Equivalent lumped circuit model for self-coupled hairpin resonator. When the sum $C_1 + C_2$ is held constant, the slope reactance and external quality factor will scale proportional to α.

that as C_2/C increases, β decreases and reduces the effect a change in coupling capacitance to the resonator (ΔC_1) would have on a change in the resonator's center frequency ($\Delta\omega_0$). This knowledge simplified the optimization process for the final filter design. When designing the filter with distributed elements (microstrip), introducing this parallel capacitance (C_2) was a key consideration.

3.5 Resonator Topology and Simulation

Ansys HFSS provided 3D EM modeling and simulation of this filter design to account for the anisotropic substrate and minor parasitic impedances not captured in the simplified ADS circuit model. The kinetic inductance in the YBCO film was approximated as less than 0.22 pH/square if operating at or below 20 K. This is a negligible contribution compared to an estimated 180 pH/square for the geometric inductance of the microstrip. As a result, a perfect elec-

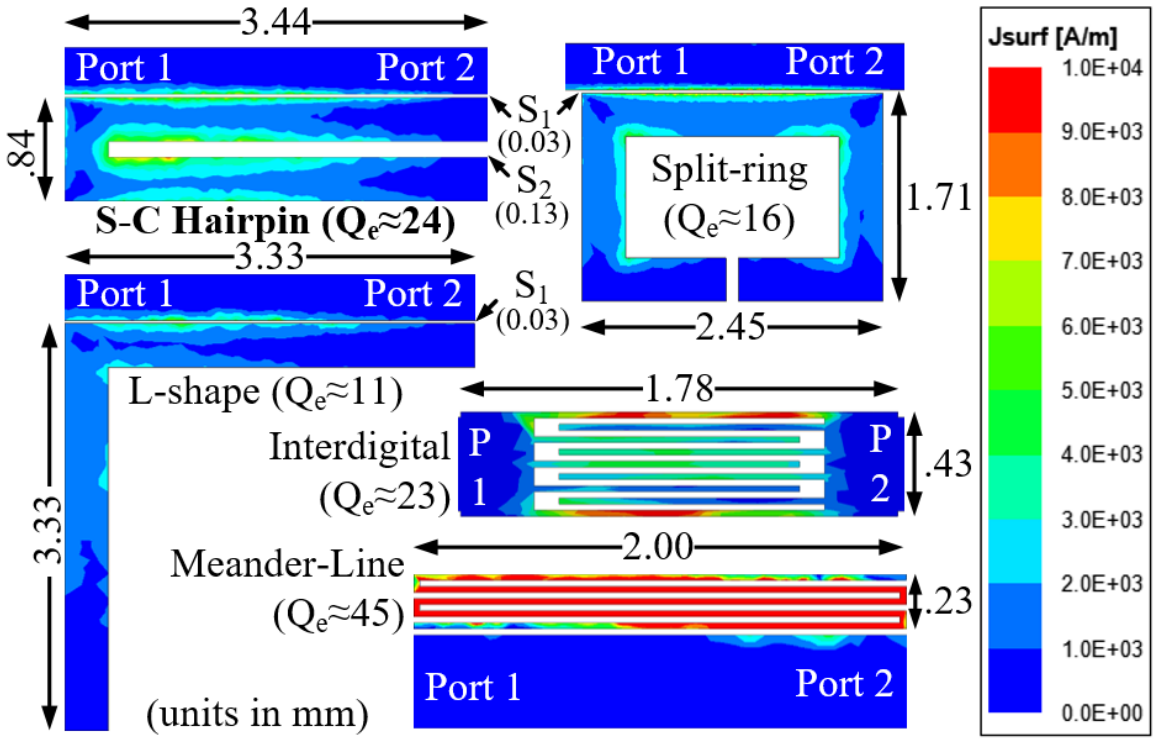

Figure 3.5: Current density for various microstrip resonator geometries

trical conducting boundary could be applied to the geometry representing the superconductor. In order to prevent a simulation error caused by the negative values in the anisotropic permittivity matrix, it is necessary to insert a thin isotropic buffer ($\varepsilon_r = 10$) on the ends of the anisotropic substrate and de-embed the waveports. This is simply a software-related issue. Fig. 3.5 shows the current density maps for a selection of various resonator geometries that were investigated for an applied 1 Watt of power at 9.4 GHz. The smaller feature sizes of the interdigital or meander-line resonators result in more fringing electric fields and increased current density, increasing the current density beyond the targeted safety margin from the estimated critical current density. The L-shape and split-ring resonator examples had a lower Q_e (set to an equivalent coupling gap) and is realized with 50 Ω transmission line. The split-ring resonator Q_e can be increased, but at the expense of expanding its width perpendicular to the transmission line.

I chose the self-coupled hairpin resonator and set the gap (S_2) at 127 μm as a trade-off between higher Q_e and lower current density. The lumped element circuit in Fig. 3.3 approximates the response of the edge-coupled (transmission line to resonator), self-coupled (between resonator arms), hairpin resonator close to its resonant frequency. Folding the microstrip resonator introduces a parallel capacitance between its arms. The effect is equivalent to introducing a capacitance C_2 in parallel to the shunt inductance L in a lumped RLC circuit. Fig. 3.6 shows the ADS simulation results for a microstrip circuit model of the self-coupled hairpin resonator at different gaps between arms and compares it with microstrip circuit models of the L-shape and split-ring resonators. Observing the Q_e plot, S_2 is chosen for its range of achievable Q_e values needed for the filter circuit model, while ensuring the current density along the edges of the microstrip did not exceed the critical current density of the thin-film YBCO. To physically realize the filter circuit, the appropriate values of S_1 are chosen from this plot. The $\Delta\omega_0$ plot highlights the additional advantage of decreasing the coupling gap between resonator arms. When S_2 is decreased, the change in resonant frequency also decreases with changing S_1. This resulted in a closer agreement between circuit and EM simulation and reduced the simulation time and number of physical parameters that needed to be optimized. Figure 3.7 illustrates the final design layout and defines its physical dimensions.

Optimizing the 3D EM model resulted in the following values as identified in Fig. 3.7: w_1 = 381 μm, w_2 = 356 μm, l = 2.2 mm, $S_{1,1}$ = 76 μm, $S_{1,2}$ = 38 μm, $S_{1,3}$ = $S_{1,4}$ = 25 μm, and S_2 = 127 μm. The final EM model incorporated multiple fabrication uncertainties which could impact filter performance. This included factors such as the circuit layout's orientation and position on the wafer. The filter layout's orientation on the substrate could result in a frequency-shift of the stop-band and the EM model enabled us to accurately predict the impact of fabrication

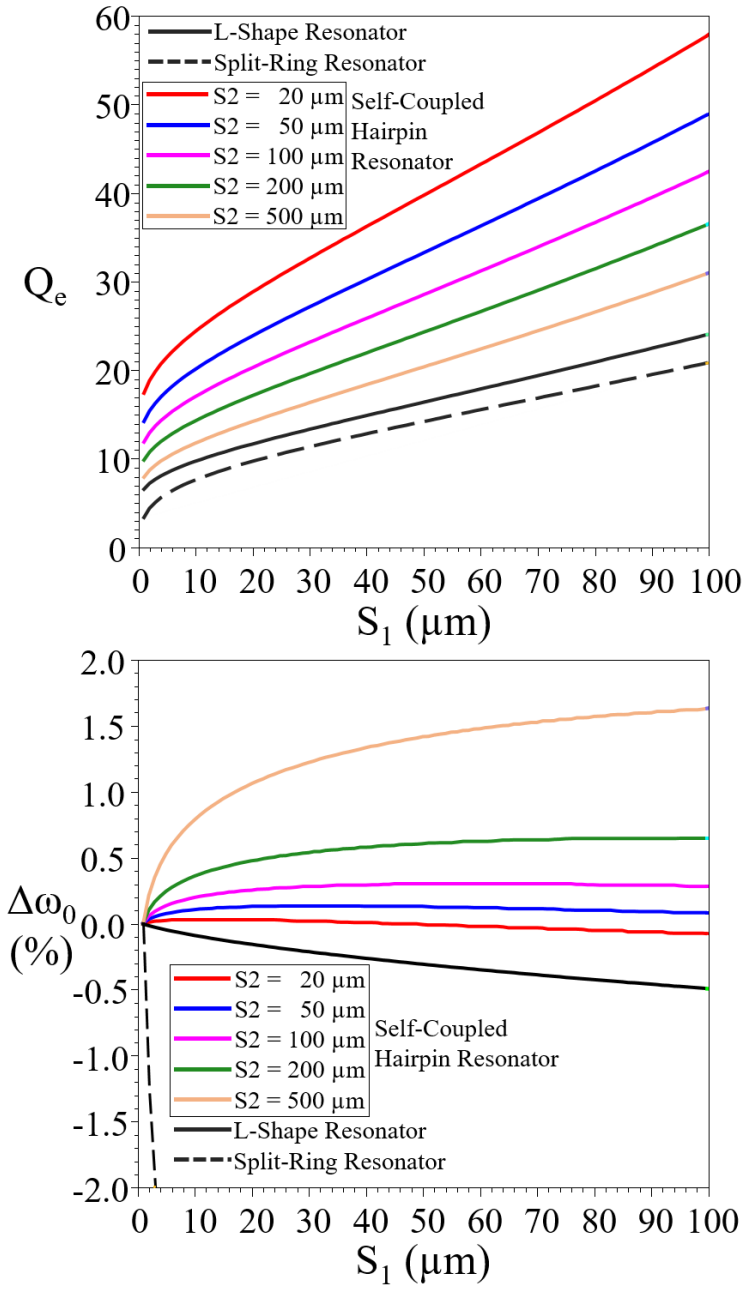

Figure 3.6: ADS microstrip circuit model simulations of external quality factor (Q_e) and shift in resonant frequency ($\Delta\omega_0$) for various resonators geometries

tolerances. Simulation results using the anisotropic permittivity matrix described in Section 3.3 agreed closely compared to a isotropic matrix using the diagonal value. There was no noticeable impact to the field line behavior or scattering parameters. However, rotating the filter circuit with

respect to the wafer such that it deviates from this permittivity matrix results in approximately a 15 MHz shift per degree of rotation. This is entirely due to the anisotropic permittivity of the substrate. The combined effect of these various factors could shift the stop-band by an amount slightly less than half of the 50 dB fractional bandwidth. In order to ensure successful fabrication of an implementable filter in the first fabrication run, I created multiple design variations where the outer arm of each resonator was lengthened or shortened by 25 μm.

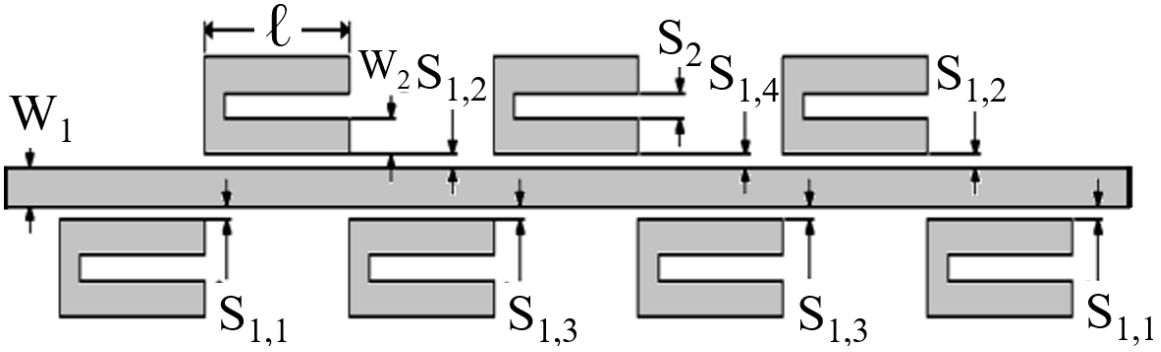

Figure 3.7: Layout of microstrip self-coupled hairpin resonator notch filter design

3.6 Experimental Results

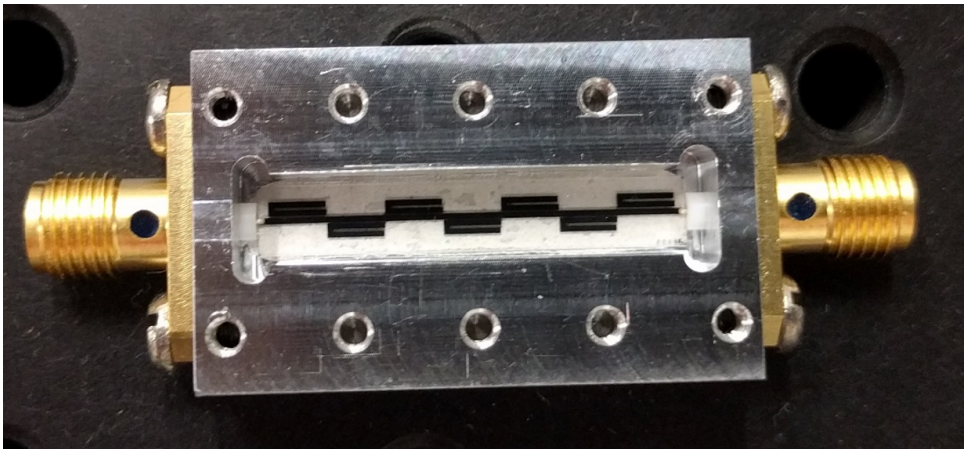

Figure 3.8: Packaged notch filter with lid removed

STAR Cryoelectronics performed the fabrication of the filter chips on a 435 μm thick R-plane sapphire wafer. The filter dimensions were patterned on thin-film YBCO with photolithography and the microstrip maintained a minimum 356 x 0.3 μm cross-section. The selected R-plane crystal orientation allowed good quality epitaxial growth of YBCO films and the substrate thickness was important for achieving 50 Ω transmission lines with physically realizable feature dimensions. For this application, the cryogenic receiver is cooled by compressed helium to 20 K and the T_c of YBCO is approximately 93 K, providing a temperature margin of around 73 K. The film quality, cross-section, wafer thickness, operating temperature, and resonator geometry enhances its capability in rejecting higher-power RFI at 9.4 GHz with acceptably low insertion loss in the lower and upper pass-bands.

After dicing the wafer into chips, the nominal design was selected and epoxied into aluminum housing with a silver epoxy (EPO-TEK EJ2189-LV) suitable for cryogenic temperatures. SMA connectors were mounted to each side and the pins were similarly epoxied to 2 μm thick Au bond pads located on each end of the microstrip. Figure 3.8 shows a picture of the final device without its lid. A Keysight VNA was used to measure the filter's insertion loss after reaching thermal equilibrium while submerged in liquid nitrogen. The VNA was calibrated for cable loss and stainless steel SMA cables were used to minimize thermal contraction in the cable length. Small changes in temperature should not impact the filter's performance. As a result, initial testing of the filter was performed with liquid nitrogen (77 K) in a laboratory environment. Figure 3.9 provides a plot of the ADS simulation results and measurement showing good agreement with the unmodified filter design. The device was tested at approximately 57 K warmer than its intended operating temperature. Modeling the expected insertion loss based on use of the Mattis-Bardeen equation to estimate the quasi-particle dissipation at the actual operating temperature results in

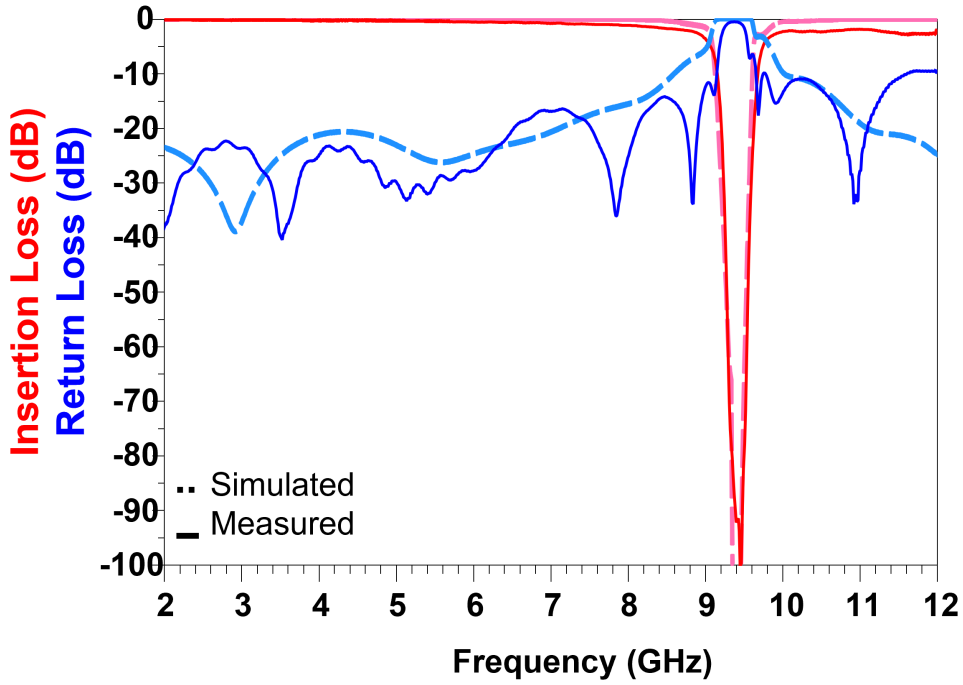

Figure 3.9: Comparison of simulated and measured insertion loss and return loss for packaged filter cooled to 77K

an approximate 2 dB insertion loss in the upper pass-band [78]. The maximum insertion loss in the lower and upper pass-bands are 0.614 dB and 2 dB, respectively. This loss is attributed to the test environment and impedance mismatch in the connector-to-chip interface as is apparent in the measured return loss at higher frequencies.

3.7 Discussion

The measured filter achieved the target fractional bandwidth and is compared in Table 1 to other published notch filter designs. Another noteworthy achievement is that this filter design achieved a higher 50 dB fractional bandwidth, but in some cases a more narrow 20 dB fractional bandwidth than previously reported measurements. This is favorable for this application where a strong stop-band rejection is required, but not a deliberately wideband design that overlaps with

Table 3.1: Comparison with previous HTS Band-Stop Filters

Ref	$\mathbf{f_c(GHz)}$	$\mathbf{\Delta f_{20dB}(\%)}$	$\mathbf{\Delta f_{50dB}(\%)}$
[79]	1.8	0.9	–
[57]	2.0	1.9	–
[80]	14.8	2.9	–
[46]	1.6	7.9	–
[81]	1.4	0.7	0.5
[49]	2.3	1.3	0.8
[48]	2.2	1.8	1.1
[51]	2.0	4.2	1.5
[50]	0.9	7.8	1.5
This Work	**9.4**	**4.3**	**2.7**

the observation bands of the radio telescope. The insertion loss is anticipated to be reduced in future testing at lower temperatures and in a revised packaging design. The measurement agrees well with simulation and confirms the estimation of kinetic inductance and insertion losses as a function of ambient temperature.

This work presents the successful demonstration of a HTS microstrip notch filter with a significant 50-dB-fractional-bandwidth notch and low insertion loss in a wide pass-band to meet the described application's strict requirements. The selection of YBCO films, substrate parameters, and resonator geometry were tailored for a consistent filter response while exposed to a local and high-power RFI source. The self-coupled hairpin resonator design enabled us to physically realize the desired filter circuit model using planar microstrip and maintain a compact footprint. Improvements to the housing design will reduce losses at higher frequencies, making this device an immediately feasible solution for GGAO's VGOS RFI mitigation needs. In a future effort, the filter chips will be assembled in a new housing design and test these devices under the correct temperature of 20 K. The SMA connectors will also be replaced with 2.92 mm connectors to provide improved higher-frequency performance and resilience to thermal cycling.

Chapter 4: Heterodyne Microwave Photonic Radiometer

This section is based on work from the following publication: C. J. Turner, A. I. Harris, T. E. Murphy and M. Stephen, "Nonlinear Power Response in Heterodyne Photonic Radiometers for Microwave Remote Sensing," in IEEE Photonics Technology Letters, vol. 35, no. 13, pp. 701-704, July 2023, doi: 10.1109/LPT.2023.3273412.

4.1 Overview

Integrated microwave photonics could play a significant role in the next generation of microwave radiometers. Microwave photonics is a field in which RF, microwave, or millimeter-wave signals are generated, distributed, processed, and analyzed using optical techniques and enables some functionalities that are not feasible with traditional electronic components [82]. Photonic integrated circuits are chip-scale optical devices used for transmitting, processing, or filtering optical signals. They have been explored for astronomy applications in the optical and near/mid-infrared regions of the EM spectrum [83]. These same technologies and signal processing techniques could be employed for microwave to sub-millimeter wavelength radiometry and spectrometry.

An ideal photonics-enabled radiometer would accurately measure weak signals over a substantially wide bandwidth ($\approx$100 GHz). The key concern with this effort is understanding the

dynamic range of a photonics-enabled radiometer. Dynamic range refers to the range of measurable microwave power between the instrument's noise floor and an upper limit set by the required linearity of its power response. The presented measurements demonstrate a significant and measurable impact to its dynamic range while taking radiometric measurements. In practice, a radiometric measurement benefits from a highly-linear calibration measurement of two temperature references. This calibration helps distinguish between a change in measured noise power from the target and detection of local fluctuations in temperature, power, or gain [2]. An accurate nonlinear model and instrument characterization can help reduce measurement uncertainty and improve the dynamic range. We show that this test radiometer exhibits a larger nonlinear response to a thermal noise signal (TNS) than to a Continuous Wave Signal (CWS) more commonly considered in literature [84]. The measurement results agree with this new stochastic nonlinear power response model and simulation.

These results will be important for developing a microwave photonic radiometer to meet the specific mission requirements. Section 4.2 discusses the state of spaceborne spectrometers of interest and photonic signal processing. Section 4.3 discusses the theory behind this improved power response model and the measurements presented in section 4.4 show strong agreement with theory. The resulting impact of these measurements on the receiver link budget analysis are illustrated and described in Section 4.5. Finally, Section 4.6 provides input on further topics to investigate.

4.2 Background

4.2.1 Spaceborne Spectrometers

NASA and NOAA have signaled the need across multiple missions for a broadband (>100 GHz) microwave radiometer that can simultaneously process the entire measured spectrum in hundreds of narrow spectral channels [85]. A microwave front-end consisting of traditional amplifiers, mixers, oscillators, and filters can channelize the measured spectrum into manageable bandwidths for digital sampling at each channel. However, increasing the system bandwidth will increase the instrument's size, weight and power (SWaP) due to the added components and additional digital spectrometers. Spaceborne spectrometers have strict SWaP requirements, limiting the performance and amount of on-board electronics available for signal processing. These constraints pose an even greater challenge at higher frequencies. At the sub-millimeter wavelength region of the EM spectrum, front-end electronic components have an intrinsically wide absolute bandwidth. For example, WR1.5 standard components covers 500-750 GHz [86]. In planetary atmosphere spectroscopy, there are molecular signatures spread across this wide band that could be measured [24]. However, past designs implement channels that down-convert and digitally process relatively narrow-band channels to measure pre-determined signatures. Table 4.1 and 4.2 highlight previous spaceborne missions and platforms containing sub-millimeter wavelength spectrometers. These instruments require some fore-knowledge of the chemical composition of the observed planetary atmosphere. A back-end spectrometer is useful for resolving narrow spectral lines. Examples of back-end architectures include Auto-Correlator Spectrometers (ACS) [87], Acousto-Optical Spectrometers (AOS) [88], and Chirp Transform Spectrometers

(CTS) [89]. Application-Specific Integrated Circuit (ASIC) digital spectrometers continue to improve in performance at low levels of power consumption, but currently at limited instantaneous bandwidths and sampling speeds [90].

Table 4.1: Examples of Spaceborne Sub-millimeter Wavelength Spectrometers

Reference	Mission Name	Instrument Name	Year Launched	Back-end Technology	Mass (kg)	Power (W)
[91]	SWAS	–	1998	AOS	102	45
[92]	Odin	SMR	2001	ACS, AOS	80	–
[93]	Rosetta	MIRO	2004	CTS	20	68
[94]	Aura	MLS	2004	ACS	453	545
[95]	SMILES	–	2010	AOS	476	320
[96]	JUICE	SWI	2022	ACS	$<$10	$<$50

Table 4.2: Spectrometer RF Performance Parameters

Reference	Instrument Name	Spectrum (GHz)	Observable Bandwidth (GHz)	Instantaneous Bandwidth (GHz)	Channel Resolution (MHz)
[97]	SWAS	487-557	16	1.4	1
[98]	SMR	118.75, 486-581	95	0.1-1	0.125-1
[93]	MIRO	190, 562	11.5	0.18	0.044
[94]	MLS	118, 190, 240, 640, 2500	21	21	0.1-96
[95]	SMILES	624-650	3.2	2.4	1.1
[99]	SWI	530-625, 1080 – 1275	8.5	2-4	0.1-16

4.2.2 Photonic Signal Processing

Photonic Integrated Circuits (PICs) were identified as a candidate technology for the next generation of microwave radiometers [100] [25]. A hybrid PIC-ASIC solution can leverage both technologies to increase a radiometer's instantaneous bandwidth, process the entire measured spectrum, and minimize additional SWaP using different back-end channel bandwidths as needed. Integrated Micro-Ring Resonators (MRR) have been implemented as tunable band-pass filters with 3-dB-bandwidths below 200 MHz [101]. The focus of this work is implementing

photonic down-conversion for digital sampling in the bands that require a finer spectral resolution than that attainable with photonic filters. Optical signal processing of radiometric microwave signals with bulk components has been applied to millimeter-wavelength signal detection [102], W-band imagery [103], and improving the noise-equivalent temperature (NET) in narrow-band radiometers [104] and radiometric resolutions in interferometers [105]. However, these efforts did not leverage the full bandwidth and integration achieved in more recent technology demonstrations. Now, integrated Electro-Optic Modulators (EOM) with CMOS-compatible voltages are capable of modulation bandwidths above 100 GHz [106]. Previous work did not extensively investigate the dynamic range of microwave photonic radiometers with photonic down-conversion. This chapter discusses and demonstrates the impact of signal type to radiometer linearity.

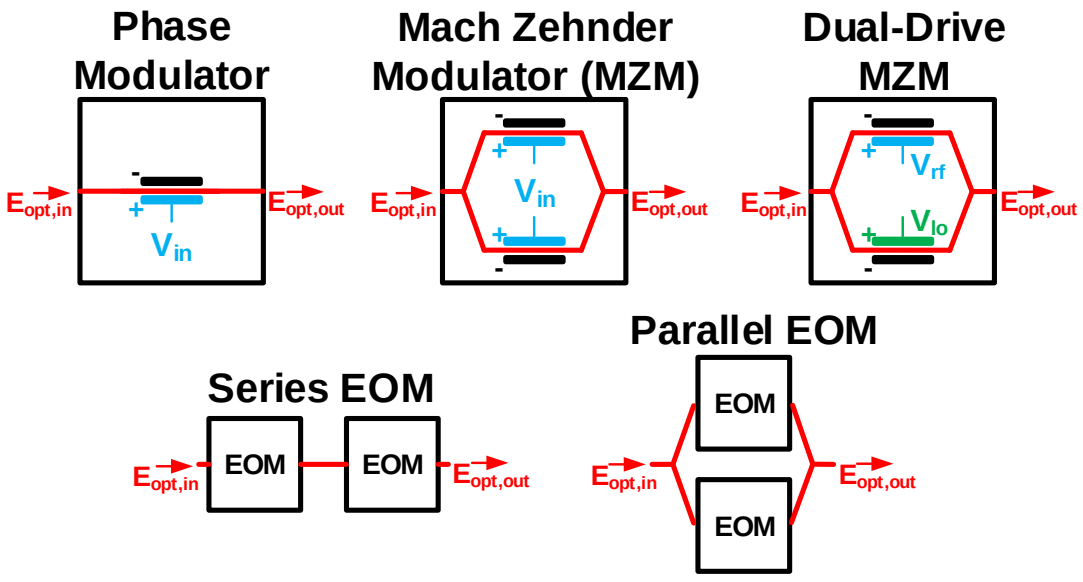

Figure 4.1: Various Electro-Optic Modulator Configurations relevant to Photonic Down-Conversion

A mixer (or down-converter) reduces the measured signal's carrier radio frequency (Ω_{rf})

to a smaller intermediate frequency (Ω_{if}) through mixing with a local oscillator frequency (Ω_{lo}). A Photonic Down-Converter (PDC) is an optical device that performs this mixing using either electro-optic modulation or optical heterodyne mixing. Multiple PDC architectures have been implemented as visualized in Figure 4.1. A phase modulator will impart a microwave signal onto the phase of an optical carrier. A Mach Zehnder Modulator (MZM) is an amplitude modulator that consists of two parallel phase-modulators. Dual-Drive MZMs (DD-MZM) and Dual-Parallel MZMs (DP-MZM) have been implemented in PDC configurations [107] [108]. In a DD-MZM, the RF and LO signal can be applied to separate, parallel phase modulators. The RF and LO signal can also be fed into parallel MZMs in a DP-MZM configuration. Other PDC configurations include cascading phase modulators or MZMs in series [84, 109, 110]. The RF-to-IF conversion loss varies for each configuration. Factors that impact the PDC gain and resulting output power include the power of the optical carrier, the responsivity of the photodetector, the operating point of the transfer function set by the DC bias, if the PDC uses a balanced photodetector (BPD), and insertion losses in the components. There are additional advantages for each configuration. For example, cascading phase modulators in series may eliminate the need for a bias stabilization circuit to optimize performance. Due to the availability of components, the theory and measurements presented here focus on the DD-MZM option.

4.3 Stochastic Nonlinear Power Response Model

A non-modulated CWS consists of a cosine function with an amplitude voltage of v:

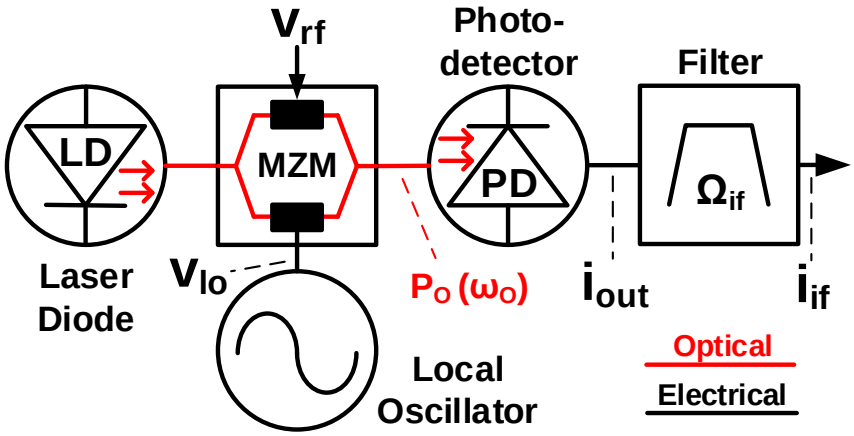

Figure 4.2: Block diagram for the single-channel microwave photonic radiometer

$$v_{\mathrm{cws}}(t) = v\cos(\Omega_{\mathrm{rf}}t + \Delta\theta) \tag{4.1}$$

where Ω_{rf} represents its frequency and $\Delta\theta$ is used to account for a potential phase offset between itself and CWS LO signal. The probability of measuring some voltage at any instant is well known for this signal and described by its probability density function (PDF):

$$f_{\mathrm{cws}}(v) = \frac{1}{\pi}(2v_{\mathrm{rms}}^2 - v^2)^{-\frac{1}{2}} \tag{4.2}$$

where v is the measured voltage and $v_{\mathrm{rms}} = \sqrt{\langle v^2 \rangle}$ is the root-mean-square (RMS) average voltage. In constrast, a TNS represents thermal noise power from blackbody radiation emissions. Its PDF follows a Gaussian or normal distribution:

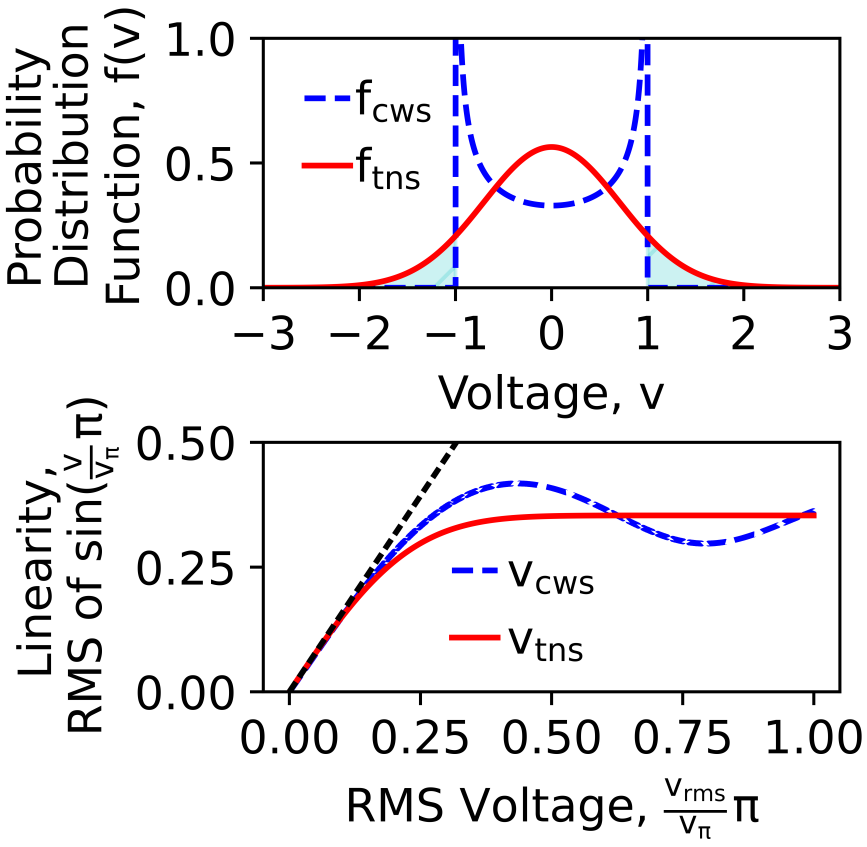

Figure 4.3: (Top) probability distribution function and (bottom) difference in linearity of Eq. 4.4 for CWS and TNS

$$f_{\text{tns}}(v) = \frac{1}{\sqrt{2\pi}v_{\text{rms}}} \exp\left(-\frac{1}{2}\frac{v^2}{v_{\text{rms}}^2}\right) \tag{4.3}$$

The differences in these PDF's are illustrated in Fig. 4.3 where f_{cws} and f_{tns} have both been constrained to share the same time-average value ($v_{\text{rms}} = 1/\sqrt{2}$). The CWS is constrained within its peak voltage of $v = 1$ and the TNS has a broader voltage distribution that exceeds this peak voltage. The probability of measuring a higher voltage with a TNS compared to a CWS is approximately 15.4%. This probability area is highlighted in cyan. When applied as an input to a nonlinear system, the average output measurement will change as a result of these different voltage distributions.

A PDC's output photocurrent is presented here [107]:

$$i_{\text{out}}(t) = \frac{1}{2} i_{\text{dc}} J_1\left(\frac{\pi}{v_\pi} v_{\text{lo}}(t)\right) \sin\left(\frac{\pi}{v_\pi} v_{\text{rf}}(t)\right) \tag{4.4}$$

The limiting component to a PDC's linearity is the EOM, so the DC photocurrent $i_{\text{dc}} = RP_0$ is taken as a constant. i_{dc} is a product of the optical power (P_0) applied to a photodetector with a responsivity (R). The key non-linear term in Eq. 4.4 is the sine function and Fig. 4.3 highlights the change in response to $i_{\text{out}}(t)$ given $v_{\text{rf}} = v_{\text{cws}}$ or $v_{\text{rf}} = v_{\text{tns}}$.

The photocurrent measured at the output of the photodetector is a summation of multiple frequency-dependent terms:

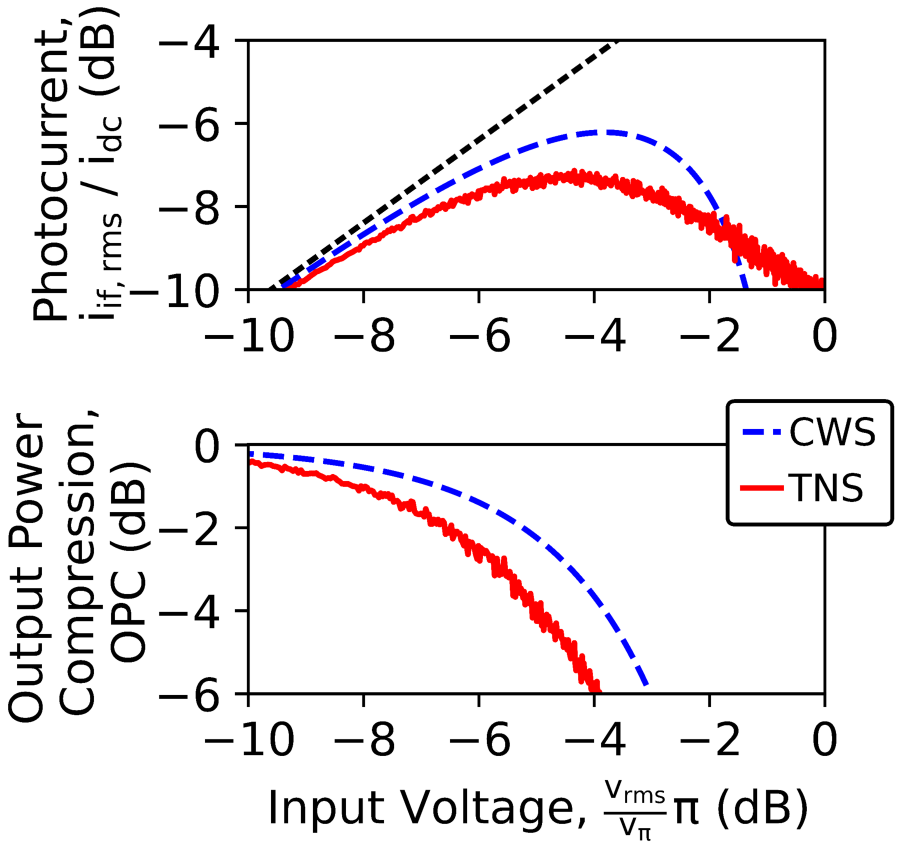

Figure 4.4: (Top) Simulated IF photocurrent and (bottom) output power compression at photodetector output

$$i_{\mathrm{out}}(t) = i_{\mathrm{dc}} + i'_{\mathrm{rf}}(\Omega_{\mathrm{rf}}t) + i'_{\mathrm{lo}}(\Omega_{\mathrm{lo}}t) + i_{\mathrm{if}}(\Omega_{\mathrm{if}}t) + ... \tag{4.5}$$

where $\Omega_{\mathrm{if}} = \Omega_{\mathrm{rf}} - \Omega_{\mathrm{lo}}$, $i'_{\mathrm{rf}}(t)$ and $i'_{\mathrm{lo}}(t)$ are leakage currents from the RF and LO signal measured at the photodetector. There are additional intermodulation products (sum-frequency, harmonics, etc) not shown here and are assumed to be suppressed through filtering. The output photocurrent (i_{out}) is filtered with an electronic band-pass filter (BPF) to isolate the desired IF term. The IF photocurrent can be determined by a numerical simulation using Fourier analysis. The Fourier analysis of random sequences has been previously discussed [111] and successfully applied in white noise models [112]. The TNS is described with the following equation:

$$v_{\mathrm{tns}}(t) = \sum_{\mathrm{k}=1}^{N/2} v_{\mathrm{k}} \cos(\Omega_{\mathrm{rf,k}}t + \phi_k) \tag{4.6}$$

With this method, the TNS is modeled as a superposition of some number of cosine terms (N), equally-spaced in frequency ($\Omega_{\mathrm{rf,k}}$), each with its own peak voltage (v_{k}) and phase (ϕ_k). ϕ_k is independently and randomly chosen over a uniform distribution from $[0, 2\pi)$ for one period. This summation has a few noteworthy advantages. Each v_{k} term can be identically distributed to correspond to white noise, or each given a mean value to more accurately model the frequency-dependent losses of the microwave components. Also, the number of samples and cosine terms can be conveniently chosen for clean conversion between the time and frequency domains in simulation using a Fast Fourier Transform (FFT).

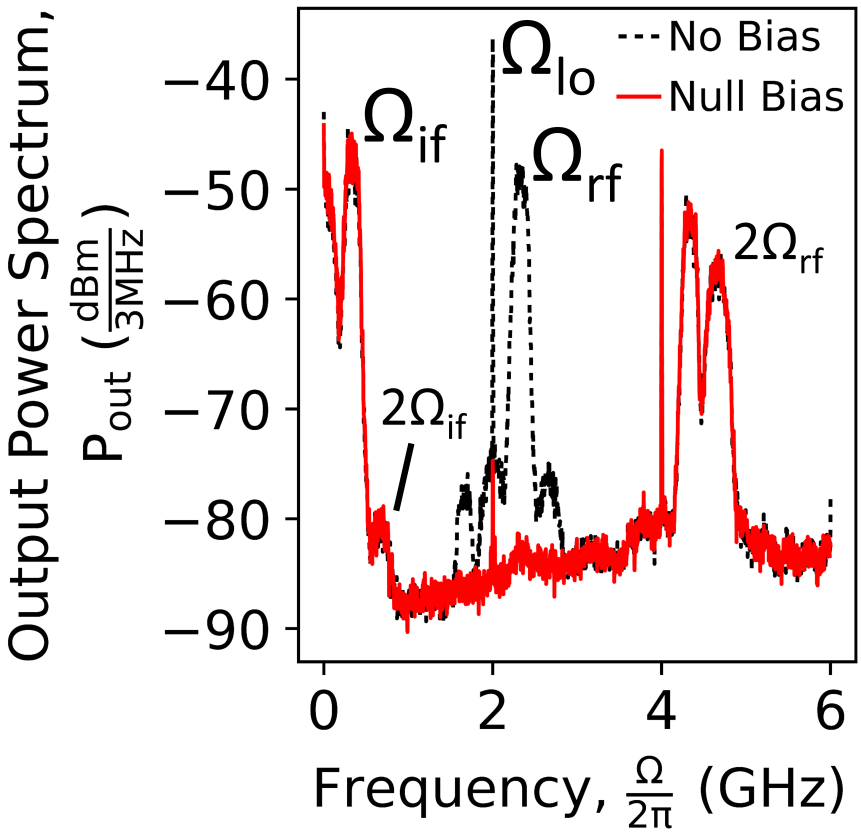

Figure 4.5: Electrical output power spectrum measured over 3 MHz resolution bins at PDC output

Fig. 4.4 presents simulation results for the IF photocurrent. i_{if} is found through a FFT of i_{out} where Eq. 4.1 and Eq. 4.6 are applied to Eq. 4.4 for a CWS and TNS signal respectively. For each value of $v_{\text{rf,rms}}$, the TNS is generated in the frequency domain with $N = 4096$ frequency terms. Each phase term is selected for one full period, which is determined by the lowest-frequency term. The voltage amplitude v_{lo} is selected to maximize i_{if}, therefore $\frac{\pi}{v_\pi} v_{\text{lo}} \approx 1.841$ and $J_1\left(\frac{\pi}{v_\pi} v_{\text{lo}}(t)\right) \approx 0.5819$. Output Power Compression (OPC) is defined as the deviation in PDC output power from a linear response to input power. It may also be referred to as gain compression since the gain is reduced from its constant small-signal-approximation value. It can be

expressed as:

$$OPC = \frac{P_{\text{if,rms}}}{P_{\text{if,rms,ss}}} = \frac{i^2_{\text{if,rms}}}{i^2_{\text{if,rms,ss}}} = \frac{G_{\text{pdc}}}{G_{\text{pdc,ss}}} \tag{4.7}$$

where $P_{\text{if,rms,ss}}$ and $G_{\text{if,ss}}$ are the small-signal, root-mean-square IF power and conversion gain for the PDC. In the same simulation, the OPC is found using this equation and plotted in Fig. 4.4. In the linear and nonlinear regions at lower voltage levels, i_{out} and OPC are in close agreement. However, the response starts to diverge prior to the OP1, the point at which the output power compresses from linearity by 1 dB.

4.4 Experimental Results

The single-channel microwave photonic radiometer was assembled with components as depicted in Fig. 4.2. It consisted of a 1550 nm DFB Laser Diode (LD), A $v_\pi = 5.5$ V Dual-Drive Mach Zehnder Modulator (DD-MZM), Photodetector (PD), and IF Band-Pass Filter (BPF). An adjustable noise source provided the TNS to the radiometer input. The noise source consists of a cascade of available amplifiers, attenuators, and filters. This noise source can produce a maximum total power of nearly 10 dBm with a center frequency of 2.3 GHz and a 3-dB-bandwidth of 140 MHz.

Fig. 4.5 presents the electrical output power spectrum of the PDC measured with a spectrum analyzer. These results demonstrate the unique behavior of this photonic radiometer using TNS instead of a modulated CWS, and compared to a traditional microwave radiometer with

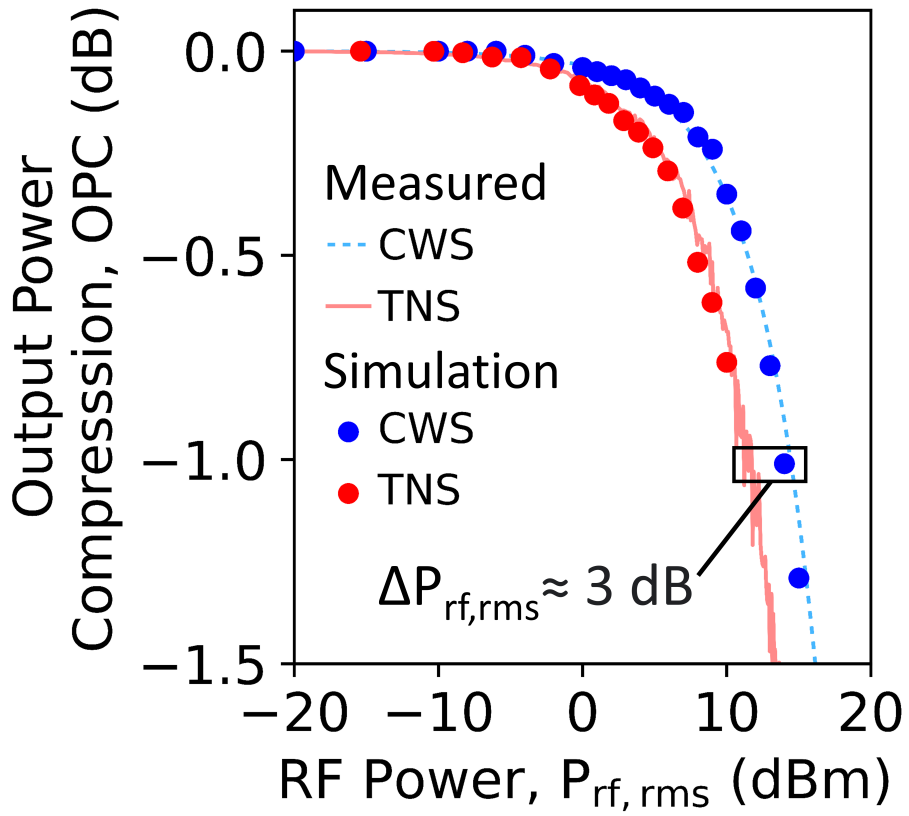

Figure 4.6: Output power compression (OPC) simulation and measurements for the IF component of the spectrum for an incident TNS and CWS

mixers. The noise source provided its maximum 10 dBm of RF power, the LD provided 16 dBm of optical power, and a signal generator provided 10 dBm of LO power. The linearity of the photodetector and spectrum analyzer detector were verified by sweeping the optical power and monitoring the measurement for a nonlinear response. The spectrum analyzer measured the power in 3 MHz bins. The IF BPF was removed for this test in order to resolve the various intermodulation products. The noise source's relatively narrow bandwidth minimized overlap of the various intermodulation products measured at the radiometer's output. There is a second-order distortion visible near DC, likely caused by rectification of the RF signal. The LO frequency was

set to 2 GHz to isolate the IF term from this distortion. The resulting IF frequency is 0.3 GHz. Leakage from the RF and LO signals are visible and identified, as well as a few other intermodulation terms. Many of these output terms can be suppressed by applying a DC bias voltage to one of the DD-MZM inputs; an unavailable option for electronic microwave mixers. Applying a DC bias to the DD-MZM so that there is a $\frac{\pi}{2}$ phase difference between modulator arms (i.e. a "quadrature" bias) will suppress even-order terms including the baseband distortion, but will also suppress the IF term. Instead, the DD-MZM can be biased to "null" (no phase difference) to suppress odd-order terms, including the RF and LO leakage terms [113]. This simplifies filtering at the output except for the baseband distortion.

We tested the PDC's nonlinear power response using both a CWS and TNS and report the results in Fig. 4.6. The measurements showed close agreement with simulation for both an applied CWS and TNS. The applied RF power for a TNS is approximately 3 dB lower than a CWS at the OP1 point of the PDC. This is a significant difference and should be taken as a design consideration for a future, complete photonic radiometer instrument. A BPF is connected to the output of a signal generator to provide a clean CWS to the DD-MZM input. The TNS output power was adjusted automatically by an Arduino-controlled digital-step attenuator. This allowed us to repeat the measurements in multiple iterations and verify there were no significant gain fluctuations over longer time scales (> 1 s). The output power was measured for both of these devices and likewise monitored for any nonlinear contributions to the final measurement. The input power was swept to the highest possible power level for our noise source and signal generator, which allowed us to measure close to the OP1. In each case, the CWS and TNS were applied to the input of the radiometer and measured the output with a BPF connected to isolate the IF photocurrent. The gain is taken as the ratio between the measured output and input powers.

Using Eq. 4.7, the resulting OPC is found by normalizing the measured gain to its small-signal gain.

4.5 Impact to Receiver Link Budget Analysis

The dynamic range is the range of signal power the radiometer can accurately measure. The lower bound is the minimum detectable signal (MDS) which is set by the noise floor. The three main contributors to the noise figure of a photonic down-converter are thermal noise, shot noise at the photodetector, and relative intensity noise (RIN) at the laser as described in the following equation [114]:

$$F_{\mathrm{pdc}} = \frac{(1+G_{\mathrm{pdc}})kT_0 + 2qi_{\mathrm{dc}}Z_{\mathrm{out}} + \mathrm{RIN}i_{\mathrm{dc}}^2 Z_{\mathrm{out}}}{G_{\mathrm{pdc}}kT_0} \tag{4.8}$$

Where k is Boltzman's constant, T_0 is the ambient temperature of the device, q is electron charge, and RIN is typically reported in unit dB/Hz. The equivalent temperature for the system is a cascade of the LNA and PDC equivalent temperatures [3]:

$$T_{\mathrm{e,sys}} = T_{\mathrm{e,lna}} + \frac{kT + 2qi_{\mathrm{pc}}Z_{\mathrm{out}} + \mathrm{RIN}i_{\mathrm{pc}}^2 Z_{\mathrm{out}}}{G_{\mathrm{lna}}G_{\mathrm{pdc}}k} \tag{4.9}$$

The upper bound of dynamic range depends on the required linearity. Here, this is described here in terms of calibration error. A Y-factor measurement is a two-point linear measurement of a hot and cold temperature reference (with respect to each other). To illustrate how linearity

can impact the calibration measurement, Figure 4.7 shows the power response of a PDC and multiple calibration lines for different scenarios. When the input signal has small bandwidth and the laser has low RIN (black dashed line), the resulting calibration line aligns strongly with the linear region of the PDC. Therefore, $T_{\mathrm{e,sys}}$ can be determined and removed from the signal measurement. At a larger bandwidth (green dashed line), the input signal to the PDC will elicit a non-linear power response. Increasing the RIN (orange and red dashed lines) will cause an even stronger non-linear response, as well as reduce the fractional change in measured power between two references. The PDC power response to a CWS is illustrated to show the impact of the stochastic model presented in this chapter. The Y-factor is defined as the difference in measured output power for two temperature references:

$$Y = \frac{P_{\mathrm{out,H}}}{P_{\mathrm{out,C}}} = \frac{G_{\mathrm{lna,H}} G_{\mathrm{pdc,H}}}{G_{\mathrm{lna,C}} G_{\mathrm{pdc,C}}} \frac{T_{\mathrm{H}} + T_{\mathrm{e,sys}}}{T_{\mathrm{C}} + T_{\mathrm{e,sys}}}. \tag{4.10}$$

If operating in the linear region of the LNA's power response, $G_{\mathrm{pdc,H}} = G_{\mathrm{pdc,C}}$ and $Y_{\mathrm{meas}} = Y_{\mathrm{ss}}$. The resulting calibration error is defined as:

$$\text{Calibration Error} = \left(\frac{T_{\mathrm{e,meas}}}{T_{\mathrm{e,sys}}} - 1\right) \tag{4.11}$$

where $T_{\mathrm{e,meas}}$ is the found from the Y-factor measurement and $T_{\mathrm{e,sys}}$ is the true noise equivalent temperature for the system.

In Figure 4.8, the excess noise figure and calibration lines are superimposed on one plot,

both a function of the LNA gain. As the LNA gain increases, the noise figure eventually converges to the noise figure of the LNA (zero excess noise figure). However, increasing the LNA gain also risks increasing the calibration error to beyond an unacceptable threshold. Reducing the sensitivity of the EOM through a lower v_π will reduce the LNA gain requirement, but will not improve the dynamic range. A better option is to increase the DC photocurrent by either increasing the optical carrier power. Another option is to reduce the relative intensity noise of the optical carrier, although this may conflict with achieving a higher amount of optical power. Currently, commercially-available 1550nm narrow-linewidth DFB lasers offer 200 mW of optical power and InGaAs photodetectors have a responsivity near 0.9 and 1.1 A/W [115]. Although the acceptable noise figure and calibration error depend on application-specific design requirements, Figure 4.8 illustrates how a low-RIN optical source is critical for minimizing the noise figure and calibration error in a wideband design.

4.6 Conclusion

This chapter covers the characterization and measurement of the power response for a single-channel microwave photonic radiometer for radiometric measurements. It also discusses the impact of these results on the link budget analysis, which shows that commercially-available components may allow for an acceptable dynamic range to meet some application-specific design requirements. In the measurements, the output power compresses by 1 dB (OP1) at nearly half the average RF input power for a thermal noise signal than for a continuous-wave signal. At higher optical powers, the noise figure of photonic down-converters are limited by the laser's relative intensity noise (RIN) [114]. There are still other impacts to performance metrics that

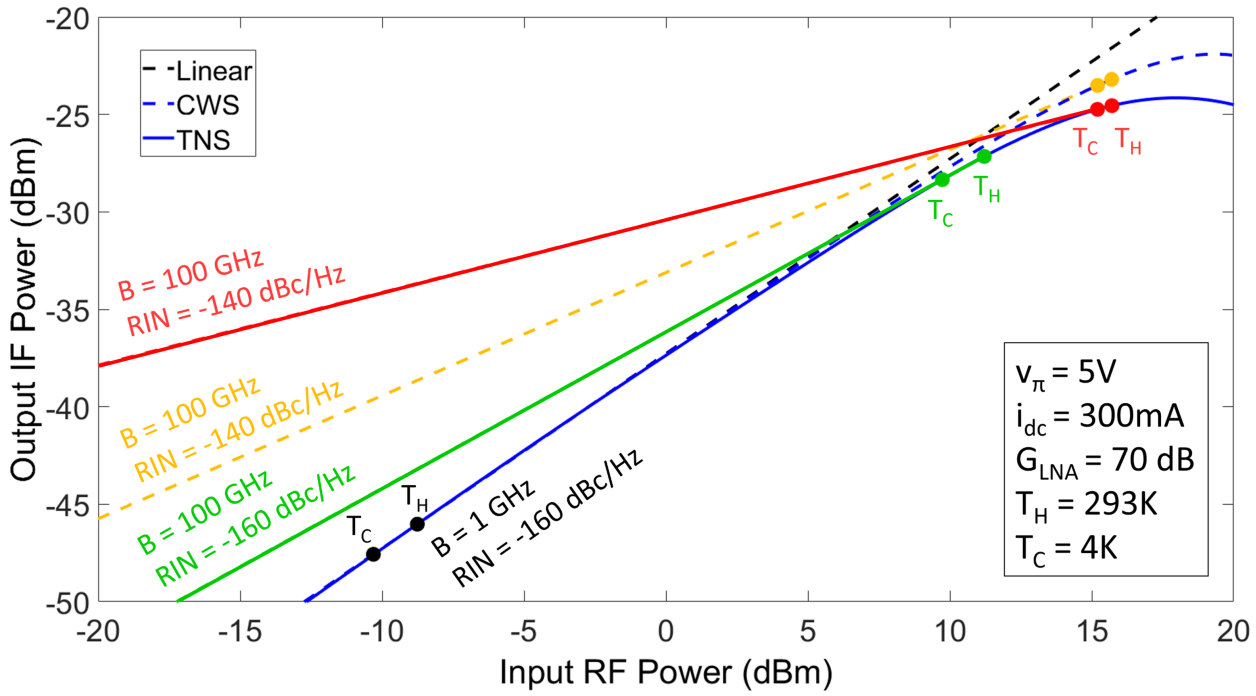

Figure 4.7: PDC power response and estimated calibration lines based on two-point Y-factor measurement with variable bandwidth and RIN.

should be explored, such as added gain fluctuations. New sources of instability from photonics could potentially impact a radiometer's performance, such as temperature drifts in the components. If some of these uncertainties have a periodic behavior, it can limit the integration time and resulting radiometric resolution.

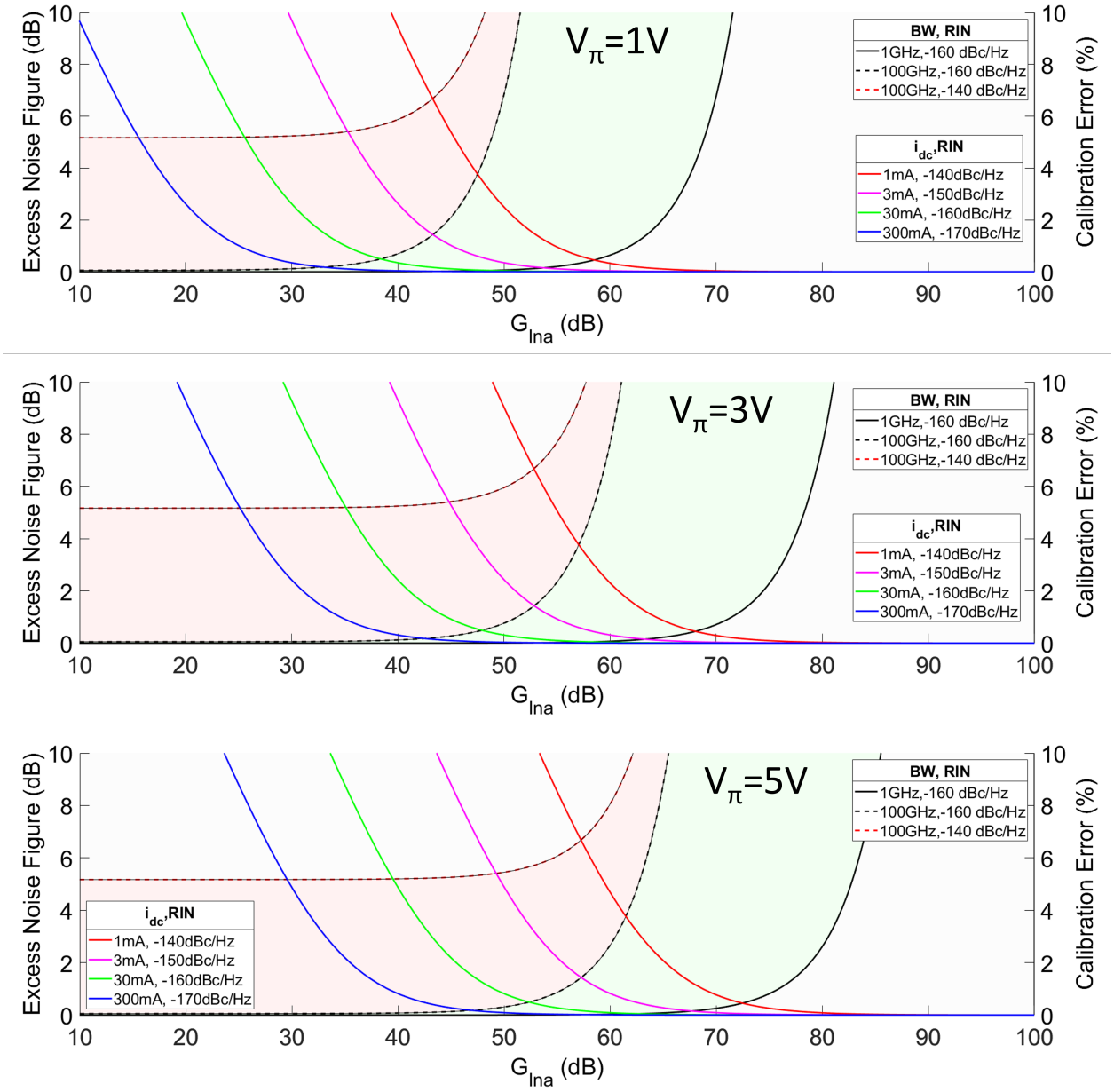

Figure 4.8: Dynamic range of a photonics-enabled radiometer with variable EOM sensitivity, bandwidth, output photocurrent, and RIN. The two reference temperatures are 4 and 293 K as in 4.7

Chapter 5: Thermal Imaging of Photonic Wire Bond

This section is based on work from the following publication: C. J. Turner, Z. Hileman, V. Rosborough, J. Musolf, H. Garrett, M. Nelson, and M. Farzaneh, "Thermal Imaging of Polymer-Based Photonic Wire Bond Through Thermoreflectance Microscopy," in IEEE Photonics Technology Letters, vol. 35, no. 20, pp. 1115-1118, 15 Oct.15, 2023, doi: 10.1109/LPT.2023.3297055.

5.1 Overview

The operation of Photonic Integrated Circuits (PIC) under extreme environmental conditions associated with aerospace industry are not well understood [116]. In order to be qualified for spaceborne instrumentation, these multi-material components may be designed and tested against harsh environmental effects and extreme operating or survivability conditions in terms of temperature, vibration, power handling, and radiation exposure. With sensitive components like micro-ring resonators (MRR), active measures such as thermal stabilization [117] and thermal cross-talk mitigation [118] may be necessary to minimize gain, wavelength, and bias drift. Due to the small feature sizes of these circuits, accurately measuring the thermal profiles of PICs will require a sub-micron thermal imaging technique. However, the diffraction limit for traditional infrared thermography precludes its use for small PIC features.

Thermal Reflectance Microscopy (TRM) is a technique that has been used to capture ther-

mal imagery of PICs with sub-micron spatial resolutions. The thermoreflectance response of a material is the relationship between a materials surface reflectively and temperature. It is measured by heating a material and measuring the change in surface reflectivity. This measurement can be used for associating changes in surface reflectivity to changes in temperature when the device is heated by other mechanisms, such as electrical or optical power. It has been successfully demonstrated on various conductors and semiconductors used in PICs [29]. However, there is limited data available on using this technique with many other materials. This chapter describes a first-time demonstration of Thermal Reflectance Microscopy (TRM) applied to a polymer-based photonic wirebond (PWB) [119]. Section 5.2 highlights the major materials involved with PICs and the previous applications of TRM to PICs. Section 5.3 describes the fabrication process and material properties of PWB. Sections 5.4 and 5.5 go over the test procedure, model, and test results and Sections 5.6 concludes with a discussion on the impact of these findings.

5.2 Background

5.2.1 PIC Materials and Integration Methods

PICs contain integrated optical circuits that can enable broadband analog radiometer and digital communication systems [82]. There have been efforts toward large-scale monolithic integration of integrated photonic components such as passive waveguides, modulators, detectors, and light sources in silicon, but silicon is not an ideal material for active components [120] [121]. Other materials exhibit superior performance for specific integrated photonic components. At 1550 nm operating wavelength, this includes indium phosphide (InP) light sources [122], lithium niobate ($LiNBO_3$) electro-optic modulators [123], InGaAs photodetectors [124], and silica (SiO_2)

or silicon nitride (Si_3N_4) waveguides [125]. Other materials such as chalcogenide glasses and polymers offer unique properties and can enable additional optical signal processing capabilities [126, 127]. Different approaches towards large-scale production of multi-material PICs include wafer-scale heterogenous integration through techniques such as wafer bonding or direct epitaxial growth [128], [129] or hybrid chip-to-chip integration through either vertical or edge coupling [130]. PWB consists of a polymer material and has demonstrated low-loss chip-to-chip coupling without requiring active alignment [119] and can also be used for integrating off-chip light sources [131].

5.2.2 Thermoreflectance Microscopy

Thermoreflectance microscopy (TRM) offers a non-invasive method of imaging the thermal profiles of photonic integrated circuit (PIC) components with sub-micron spatial resolutions [29]. This is important for the detection of hot spots, ensuring reliable device design and consistent fabrication. Traditional infrared (IR) thermography is achieved through passive imaging of blackbody radiation emissions with mid-wavelength IR (MWIR) cameras. The spatial resolution of these detectors are limited by the diffraction limit of their operating wavelengths where they have an acceptable sensitivity (typically around 3 μm). TRM is an indirect measurement of a device's thermal profile. In this technique, the relative change in surface reflectivity is measured as it changes with temperature. The thermoreflectance properties for a semiconductor relates back to its band structure and dielectric response function [132]. TRM has been used successfully to obtain thermal profiles of semiconductor optical amplifiers, electro-absorption modulators, and various laser diode devices, among others [29].

Time Domain Thermoreflectance (TDTR) measurement techniques have been used to characterize the thermal properties of various polymers [133], including SU-8 photoresist [134]. This technique uses a pump laser to induce a temperature strain at the surface of a material caused by optical absorption. A second probe laser measures the change in surface reflectivity. In contrast, TRM uses an LED and camera in place of the probe laser and detector to capture a larger image. However, TRM has not been applied to an acrylate-based photonic device for imaging a thermal profile. Although optical absorption of telecomm-band optical wavelengths are relatively small ($<$1 dB/cm) [135], nano-scale structures are still susceptible to heating by relatively high levels of optical power ($>$100 mW). These particular structures are also free-standing, lowering the maximum optical power that they can handle. The dimensions of these devices are small enough such that passive IR thermography cannot provide the necessary spatial resolution for hot spot detection and predictive failure analysis. Our results demonstrate TRM's capability in characterizing the thermal profiles of more complex photonic architectures, encourages future investigations into applying TRM to other polymer-based devices, and reinforces the use of TRM for high-resolution thermography of multi-material PICs.

5.3 Device Characteristics

Photonic wire bonding was first demonstrated using a SU-8 core (n = 1.57 at 1550 nm) with a Cytop cladding (n = 1.34 at 1550 nm) [119]. Currently, Vanguard Automation offers the SONATA tool to fabricate PWB using its proprietary material, VanCore A [136]. This material is an acrylate-based resin with optical and thermal properties similar to SU-8 negative photoresist. For the optical absorption and heat transfer model discussed in Section 5.5, the physical parame-

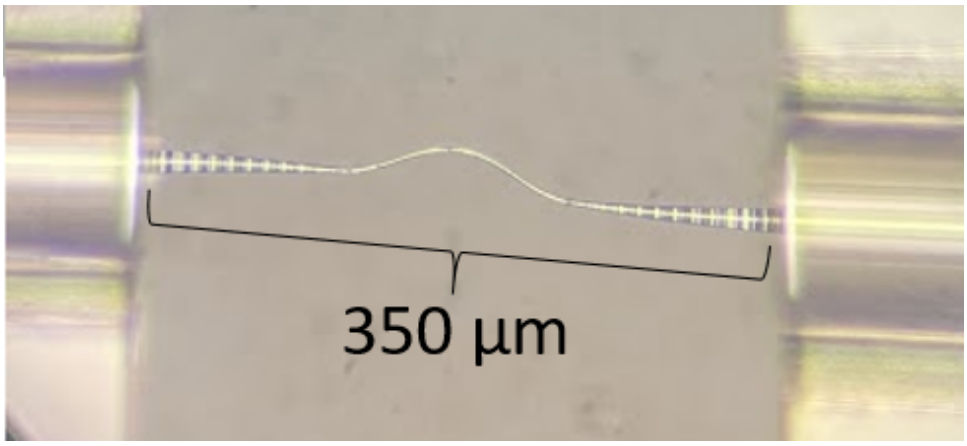

Figure 5.1: Photonic Wire Bond (PWB) connected to fiber array channels.

ters used include an optical absorption of 0.5 dB·cm^{-1}, density of 1190 kg·m^{-3}, specific heat of 1.5 kJ·kg^{-1}·K^{-1}, and a thermal conductivity of 0.3 W·m^{-1} [137].

PWB are fabricated using direct-write 3D laser lithography based on two-photon polymerization [119]. Individual pixels are fixed to a common mount using pick-and-place machinery with relatively moderate precision. The interconnect regions are embedded in the photo-resist material and the positions of the connecting facets are detected using machine vision techniques. The PWB structure is designed with respect to the facet positions and defined using two-photon lithography. In the next step, the unexposed photo-resist is removed. The remaining PWB structures are embedded in a low-index cladding material [136]. This eliminates the need for active alignment between chips and PWB can handle different mode fields of connected devices. The specific devices discussed in this chapter were fabricated and supplied by Freedom Photonics Inc. [115]. These devices did not have cladding as recommended in the last step of the fabrication process in the interest of another related research effort. Instead, they are suspended in air. Through conversations with Vanguard Automation and power testing of other devices, the major anticipated consequence of this is a reduction in power handling.

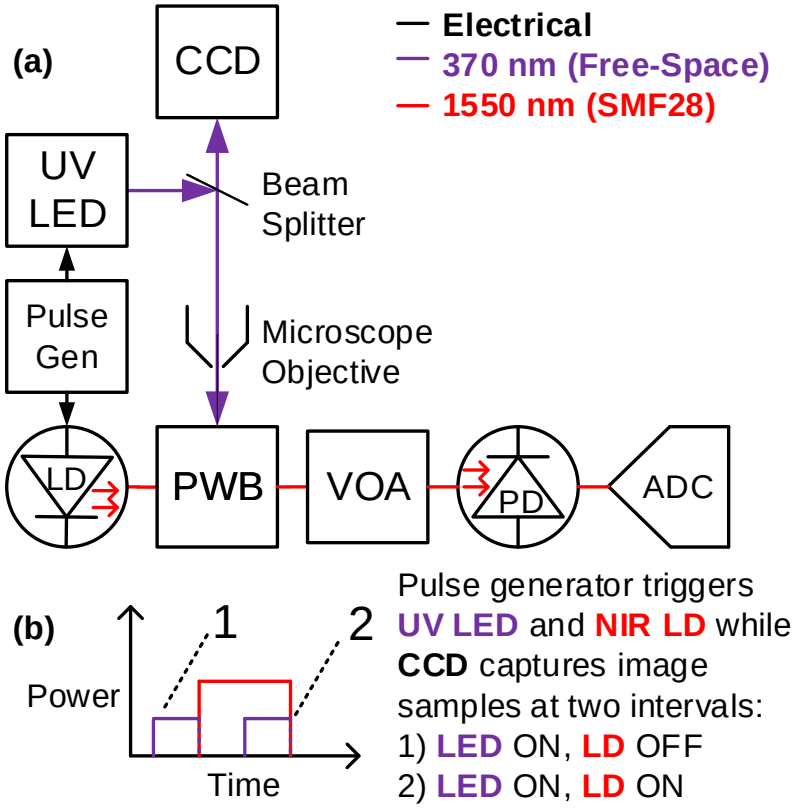

Figure 5.2: (a) TRM test schematic where an Ultra-Violate Light-Emitting Diode (UV LED) illuminates and a Near-Infrared Laser Diode (NIR LD) powers a Photonic Wire Bond (PWB) test device. A Charge-Coupled Device (CCD) Camera captures image samples and a Photo-Detector (PD) and Analog-to-Digital Converter (ADC) monitors the NIR optical signal. (b) Plot of power pulses to LD and LED showing the relative timing of these pulses.

5.4 Test Procedure

TRM is based on the relationship between the measurable relative change in surface reflectivity ($\Delta R/R$) with a change in temperature (ΔT) as described in the following equation [29]:

$$\Delta T = \kappa^{-1} \frac{\Delta R}{R} \tag{5.1}$$

where κ is thermoreflectance calibration coefficient, which depends on the material of the surface and wavelength of the illuminating source. Figure 5.2 shows the schematic of the experimental setup of the test component shown in Figure 5.1. The PWB is the device under test and is illuminated with a 370-nm-wavelength ultra-violet Light Emitting Diode (UV LED) while imaged with a 1.4MP, 12-bit Thorlabs CCD Camera mounted on a standard microscope assembly. TRM measurements in this work are based on the technique described in detail in references [138–142]. As illustrated by the diagram in Figure 5.2, a pulse generator is used to pulse both the illumination UV LED and a 1550 nm laser diode (LD). As illustrated in Figure 5.2, the CCD captures images while the UV LED is pulsed to illuminate the surface of the device. The UV LED fits a standard T-1 3/4 package and was pulsed with a drive current of 30 mA for a resulting forward optical power of approximately 2 mW. The 1550 nm LD powers the fiber-coupled device under test and acts as the heating pulse. A controllable time delay between the UV LED and the LD allows two images to be obtained by the CCD camera: one before the heating pulse (the "off-image") and one during the heating pulse, after allowing for the device to reach thermal equilibrium (the "on-image"). The difference between these two images divided by the "off-image", is a measure of the relative change in surface reflectivity, as shown in Eq. 5.1. Each image is then averaged over at least 10,000 heating and cooling cycle to improve the signal-to-noise ratio. The variable optical attenuator (VOA), photodetector (PD), and analog-to-digital converter (ADC) were used to measure the output optical power (without saturating the

PD) and to ensure the overall correct operation.

The LED wavelength was chosen as a trade-off; the CCD camera is more sensitive at visible wavelengths, but the PWB material is too transparent in this spectrum to measure a clear response. Previous studies have successfully used UV light to image SU-8 [143]. In order to obtain the thermoreflectance calibration coefficient (κ), the thermoreflectance response of a 200x200 μm bulk sample of the PWB material was measured under 370 nm illumination based on the technique used in [144, 145]. Since the anticipated temperature change was less than 10°C for the device under test, a calibration coefficient value of $k = -2.4 \cdot 10^{-4}$ K^{-1} was extracted at this range of temperature change. However, because of the low sensitivity of the CCD camera at this wavelength, it is speculated that this value for the calibration coefficient might not be very accurate for larger temperature changes. Further work at different illumination intensities and wavelengths are needed to obtain a more accurate value for the calibration coefficient.

5.5 Experimental Results

The test device consisted of two 8-channel fiber arrays mounted on a glass slide. The PWB's were designed to connect each channel of the fiber array. Each PWB is approximately 350 μm in total length, as shown in Fig. 5.1. The cross-section diameter is 20 μm near the interface and 2 μm at the center and spanning over a 100 μm length along its waist. A DFB laser pulsed the test device with 40 mW of optical power over a 2.5 ms pulse width and a 10 ms period. The thermoreflectance signal was measured according to the procedure outlined in Section 5.4.

There were a number of key concerns explored for this measurement. In order to address the potential for measuring a fluorescent response, 3 PWB were imaged with a 10x objective

while LD power was only applied to the middle PWB. The image is presented in Figure 5.3, where it is clear that only the powered PWB has a measurable response. Another concern was the potential for measuring LD-emitted light (1550 nm) scattered from the PWB. An NIR filter was placed in front of the CCD Camera and it was also confirmed that even without the filter, the contribution of any LD-emitted light is negligible due to the low sensitivity of the CCD camera at 1550 nm. To verify this, the thermoreflectance image was separated from the LD-emission image based on the pulsing technique described in [146]. The LD emission contribution is negligible as shown in Figure 5.3(c). SU-8 photoresist has a higher optical absorption at UV wavelengths than near infrared (NIR) wavelengths [135]. The measured normalized surface reflectivity predominantly changed between 0 and -0.02. Because of the change in height deviation across the PWB, the focus was set on the right side of the image where the optical power was applied. The center of the PWB shows an equal positive and negative change in surface reflectivity on either side along its length. However, this region was out of focus and most susceptible to movement between the camera and stage. In future tests, a tilted stage and additional stabilization measures could improve accuracy.

Applying TRM to this device resulted in significantly improved image spatial resolution. As a point of comparison, an equivalent PWB structure was imaged on a Mid-Wavelength Infrared (MWIR) microscope setup using a cryogenically-cooled MWIR camera and 15x objective. In order to compensate for the camera's sensitivity, the entire device was heated to an ambient temperature of 65°C. When powered at a continuous 40 mW, the device heated to a peak 5°C above ambient temperature. Using this result, the estimated optical absorption is approximately 0.5 dB/cm and is similar to SU-8 [135]. During the TRM measurements, the device temperature was actively controlled at a lower 25°C using a TEC module. Figure 5.4 shows the difference in

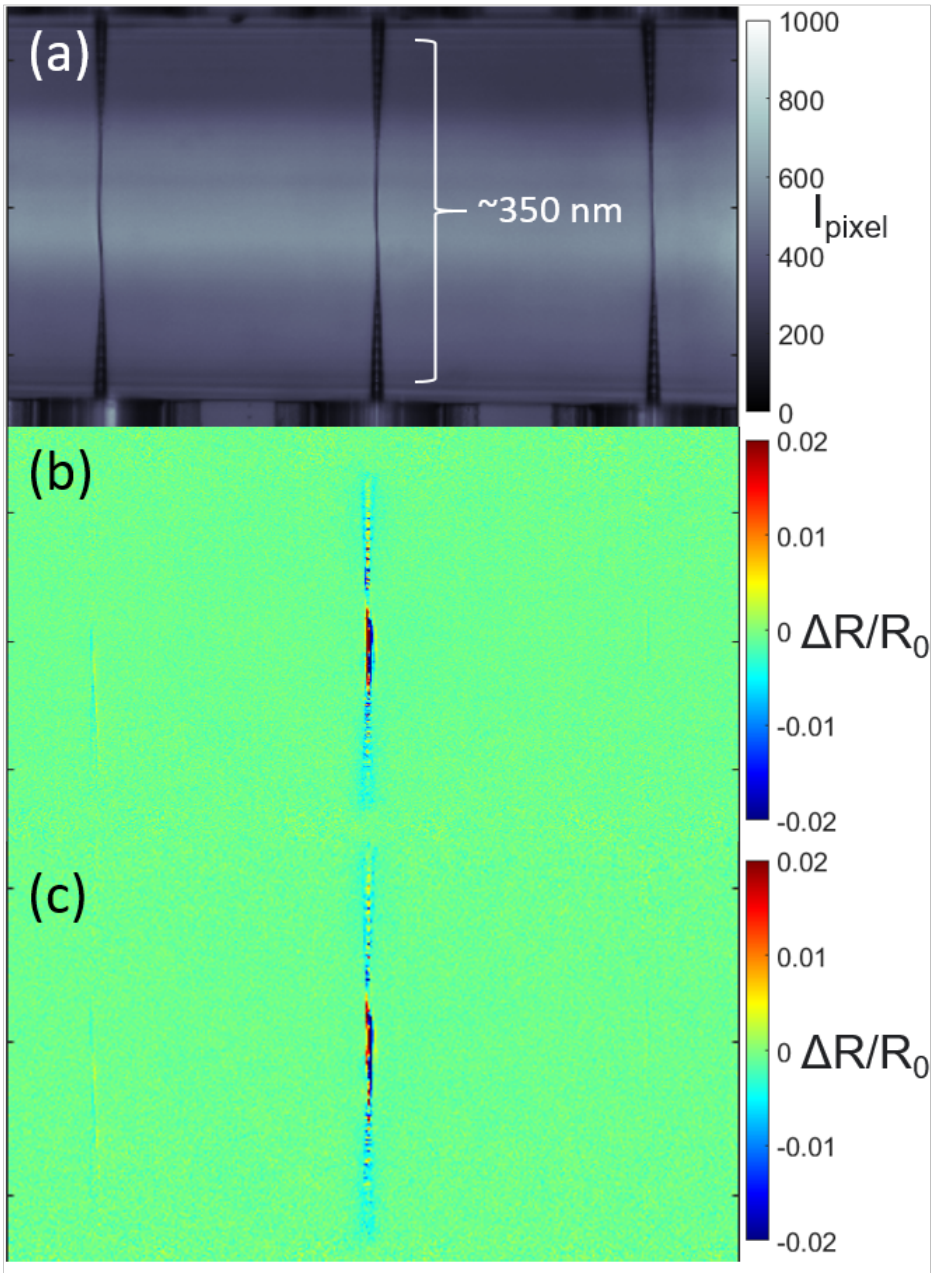

Figure 5.3: Images of PWB measured with a 10x objective where only the center device is powered, including (a) camera pixel intensity (I_{pixel}), (b) measured surface reflectivity, (c) surface reflectivity with LD emissions removed.

image resolutions while measuring MWIR (a and b) and thermoreflectance (c and d) using a 20x (c) and 100x (d) microscope objective. With the 100x objective, the image ultimately achieved a 75 nm pixel resolution for this image and estimate the diffraction-limited spatial resolution as below 300 nm using the Rayleigh criterion and neglecting mechanical vibrations. The enhanced resolution of TRM reveals temperature gradients in the PWB taper over features resulting from additional exposure during the polymerization process.

The TRM and MWIR results agree closely with simulation. Figure 5.5 presents the average temperature over the cross-sectional thickness of the PWB, measured along the longitudinal section of the PWB from input to output. The measured TRM results are compared against the MWIR measurement and a COMSOL simulation. The simulation contains a 3D CAD model for the PWB and numerically solves for optical absorption and heat-transfer in an SU-8-based medium using Beer-Lambert's law and the finite element method [147]. The medium is surrounded by a volume of air and the outer-most boundaries are set to ambient temperature as verified in measurement. In this simplified solution, the input and output interface boundaries are set to ambient temperature as a substitute for modeling the transition from fiber. The MWIR data is taken from Figure 5.4(a) and the TRM data is from two separate measurements under 100x magnification. It is clear from these measurements that the hottest regions of the PWB are these tapers, with the coolest regions at the interface and center of the PWB. Test equipment was unavailable to pulse the device at higher optical powers, but a future effort should include increasing power to predict and identify points of failure.

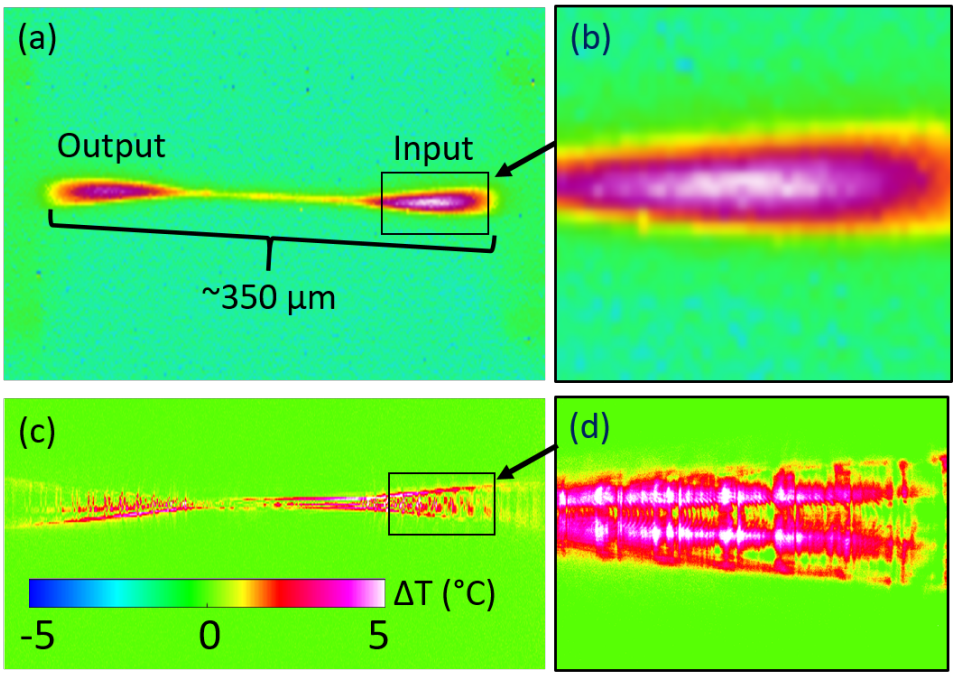

Figure 5.4: Thermal profiles of PWB taken with different techniques: (a) original and (b) expanded MWIR image with 65°C ambient temperature. TRM image with (c) 20x objective and (d) 100x objective with 25°C ambient temperature. TRM with 100x objective achieved 75 nm pixel resolution.

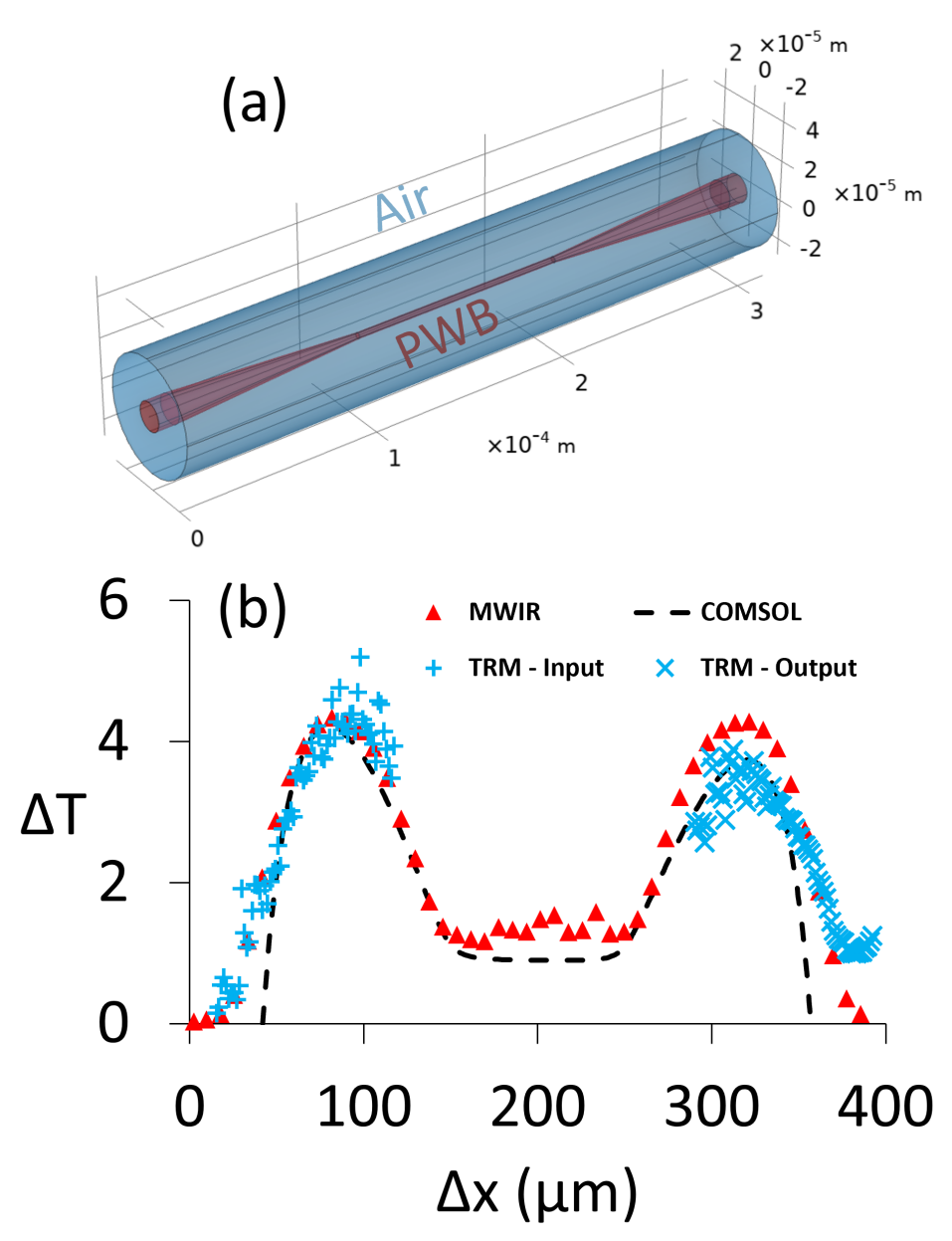

Figure 5.5: (a) COMSOL 3D CAD model and (b) average temperature difference (ΔT) along longitudinal cross-section offset (Δx) from input facet of PWB.

5.6 Discussion

The thermal profile for PWB with a sub-micron spatial resolution was successfully captured using TRM. PWB is a photonic component consisting of an acrylate-based resin with material properties similar to SU-8 negative photoresist. These devices are fabricated using a two-photon polymerization process. These results demonstrate the feasibility of using TRM for polymer-based PIC features and encourage investigating other relevant materials beyond semiconductors and metallic electrodes. Polymers offer unique properties for photonic integrated circuits and this measurement technique could be applied to acquire thermal imagery for multiple polymer-based photonic devices and interconnects, such as electro-optic modulators [148], tapered polymer fibers [149], and vertical couplers [150]. When applied to more complicated structures, this analysis can provide a useful tool for predicting points of failure and creating more environmentally-robust PWB and overall PIC designs. In these measurements, it was verified that there was no flourescence or NIR scattering. Our results also showed close agreement with simulation and traditional MWIR measurements. Future investigations include testing these components at other LED and LD wavelengths, with higher-power LED's and LD optical pulses, and with additional measures to bring the entire device into focus.

Chapter 6: Conclusion

6.1 Summary

Three different technology development efforts were presented for the advancement of radiometer technology. The first topic is the design, fabrication, and testing of a thin-film superconducting notch filter with a 4.3% 50-dB-fractional-bandwidth centered on 9.4 GHz. The filter topology was chosen to handle the power intercepted by the side-lobe of a high-power, local RFI source. Through measurement, it was demonstrated the operating band extended from 2-12 GHz. The insertion loss increases at higher frequencies and this is attributed to the testing temperature and mismatch in the packaging. Still, the filter demonstrates fantastic performance compared to other thin-film high-temperature superconducting designs.

The second topic presents a new nonlinear power response model to account for the nature of the received thermal noise signal in a photonics-enabled microwave radiometer. Through theory and measurement, it's demonstrated that the point where the output power deviates from linearity by 1 dB, is 3 dB lower than it would be with a traditional continuous wave signal. Photonic down-convertors have relatively high noise contributions that are limited by the laser's relative intensity noise. To compensate for this, a high-gain low-noise amplifier (LNA) will help maintain a low noise-equivalent temperature for the radiometer. However, having a high gain risks driving the photonic down-converter into a non-linear region of operation. The model pre-

sented helps demonstrate the trade-off in noise-equivalent temperature and linearity as a function of the electro-optic modulator sensitivity, output photocurrent, and LNA gain.

The third topic is the thermal imaging of photonic wire bond using themo-reflectance microscopy (TRM). This is a first-time demonstration of this measurement technique on a polymer-based photonic device. These results encourage its use in measuring the thermal profiles of multi-material PICs. This could lead to more robust designs for operation in a spaceborne photonics-enabled microwave radiometer.

6.2 Future Directions

The work presented in this thesis can branch off in multiple directions. A new package has been designed and fabricated for installation of the superconducting notch filter chip. After assembly, the device can be tested at its intended operating temperature (20 K) and should demonstrate improved insertion loss out to 14 GHz. The photonics-enabled radiometer non-linear power response model can be fed used to improve simulation accuracy in a more complete instrument such as The Hyperspectral Microwave Photonic Instrument (HYMPI) [25]. This work could expand into system-level design where multi-channel architectures could be explored. One key PIC-unique technology for multi-channel down-conversion could be integrated optical combs [151]. Leveraging this technology, unique LO signals for each channel could be generated so each channel is simultaneously down-converted to baseband for digital processing.

The TRM results could also continue on several different paths. More data should be collected for photonic wire bond at different power levels, illuminating wavelengths, and ambient temperatures. According to the vendor Vanguard Automation, it is anticipated that the mate-

rial may fluoresce under certain conditions and it is unknown how linear the thermo-reflectance response should be over a greater temperature range. There is limited data available on using this technique for non-linear crystals and other polymers. Thin film lithium niobate currently appears as a leading option for wideband, integrated electro-optic modulators [152]. In order for thermo-reflectance microscopy to be a feasible option for thermal imaging of multi-material PICs, exploring this technique with lithium niobate should be a next step.

Appendix A: Publications

Peer-Reviewed Journal Articles

C. J. Turner, Z. Hileman, V. Rosborough, J. Musolf, H. Garrett, M. Nelson, and M. Farzaneh, "Thermal Imaging of Polymer-Based Photonic Wire Bond Through Thermoreflectance Microscopy," in IEEE Photonics Technology Letters, vol. 35, no. 20, pp. 1115-1118, Oct 2023

C. J. Turner, A. I. Harris, T. E. Murphy and M. Stephen, "Nonlinear Power Response in Heterodyne Photonic Radiometers for Microwave Remote Sensing," in IEEE Photonics Technology Letters, vol. 35, no. 13, pp. 701-704, Jul 2023

C. J. Turner, T. Stevenson, R. Cantor, L. Hilliard, T. E. Murphy and B. Bulcha, "Superconducting Notch Filter for RFI Mitigation in Ground-Based Radio Telescope," in IEEE Transactions on Applied Superconductivity, vol. 33, no. 3, pp. 1-5, Apr 2023, Art no. 1100605

D. J. Kline, M. C. Rehwoldt, C. J. Turner, P. Biswas, G. Mulholland, S. McDonnell, and M. Zachariah. "Spatially focused microwave ignition of metallized energetic materials," Journal of Applied Physics, vol. 127, no. 5. AIP Publishing, Feb. 2020.

Conference Proceedings

C. Turner, M. Stephen, F. Gambini, G. Chin, P. Racette and T. Murphy, "Ultra-Wideband Photonic Radiometer for Submillimeter Wavelength Remote Sensing," 2020 International Topical Meeting on Microwave Photonics (MWP), Matsue, Japan, 2020, pp. 124-127

Bibliography

[1] Bernard F. Burke, Francis Graham-Smith, and Peter N. Wilkinson. *An Introduction to Radio Astronomy*. Cambridge University Press, July 2019.

[2] Fawwaz Ulaby and David Long. *Microwave Radar and Radiometric Remote Sensing*. The University of Michigan Press, 2014.

[3] J. J. Condon and S. M. Ransom. *Essential Radio Astronomy*. Princeton Series in Modern Observational Astronomy. Princeton University Press, 2016.

[4] Geoffrey A. Blake, E. C. Sutton, C. R. Masson, and T. G. Phillips. Molecular abundances in OMC-1 - the chemical composition of interstellar molecular clouds and the influence of massive star formation. *The Astrophysical Journal*, 315:621, Apr 1987.

[5] Paul Racette and Roger H. Lang. Radiometer design analysis based upon measurement uncertainty. *Radio Science*, 40(5):n/a–n/a, September 2005.

[6] K. G. Jansky. Electrical disturbances apparently of extraterrestrial origin. *Proceedings of the Institute of Radio Engineers*, 21(10):1387–1398, 1933.

[7] Grote Reber. Notes: Cosmic static. *Astrophysical Journal*, 91:621–624, 1940.

[8] C. Hazard, M. B. Mackey, and A. J. Shimmins. Investigation of the radio source 3c 273 by the method of lunar occultations. *Nature*, 197(4872):1037–1039, 1963.

[9] A. Hewish, S. J. Bell, J. D. H. Pilkington, P. F. Scott, and R. A. Collins. Observation of a rapidly pulsating radio source. *Nature*, 217(5130):709–713, 1968.

[10] H. I. Ewen and E. M. Purcell. Observation of a line in the galactic radio spectrum: Radiation from galactic hydrogen at 1, 420 mc./sec. *Nature*, 168(4270):356–356, 1951.

[11] A. A. Penzias and R. W. Wilson. A measurement of excess antenna temperature at 4080 mc/s. *Astrophysical Journal*, 142:419–421, 1965.

[12] The CHIME/FRB Collaboration. A bright millisecond-duration radio burst from a galactic magnetar. *Nature*, 587(7832):54–58, Nov 2020.

[13] A. W. Straiton, C. W. Tolbert, and C. O. Britt. Apparent temperatures of some terrestrial materials and the sun at 4.3-millimeter wavelengths. *Journal of Applied Physics*, 29(5):776–782, 1958.

[14] Jet Propulsion Laboratory (U.S.), United States National Aeronautics, and Space Administration. *Mariner-Venus, 1962 : final project report*. Scientific and Technical Information Division, National Aeronautics and Space Administration : United States Government Printing Office Washington, D.C., 1965.

[15] A. E. Basharinov and A. M. Shutko. Research into the measurement of sea state, sea temperature and salinity by means of microwave radiometry. *Boundary-Layer Meteorology*, 18(1):55–64, 1980.

[16] NASA Goddard Space Flight Center. *The Nimbus 5 User's Guide*. National Technical Information Service, 1972.

[17] R. A. Kroodsma, M. A. Fritts, J. F. Lucey, M. R. Schwaller, T. J. Ames, C. M. Cooke, and L. M. Hilliard. Cosmir performance during the gpm olympex campaign. *IEEE Transactions on Geoscience and Remote Sensing*, 57(9):6397–6407, 2019.

[18] Clive Rodgers. Satellite remote sensing: The retrieval problem. In Guy Brasseur, editor, *The Stratosphere and Its Role in the Climate System*, pages 133–171, Berlin, Heidelberg, 1997. Springer Berlin Heidelberg.

[19] R. M. Fano. Theoretical limitations on the broadband matching of arbitrary impedances. *Journal of the Franklin Institute*, 249(1):57–83, January 1950.

[20] A. Richard Thompson, T. E. Gergely, and P. A. Vanden Bout. Interference and Radioastronomy. *Physics Today*, 44(11):41–49, 11 1991.

[21] John M. Ford and Kaushal D. Buch. RFI mitigation techniques in radio astronomy. In *2014 IEEE Geoscience and Remote Sensing Symposium*. IEEE, July 2014.

[22] Yang Liu, Amol Choudhary, David Marpaung, and Benjamin Eggleton. Integrated microwave photonic filters. *Adv. Opt. Photon.*, 12(2):485–555, Jun 2020.

[23] J. W. Waters. Submillimeter-wavelength heterodyne spectroscopy and remote sensing of the upper atmosphere. *Proceedings of the IEEE*, 80(11):1679–1701, 1992.

[24] C. Turner, M. Stephen, F. Gambini, G. Chin, P. Racette, and T. Murphy. Ultra-Wideband Photonic Radiometer for Submillimeter Wavelength Remote Sensing. In *2020 International Topical Meeting on Microwave Photonics, MWP 2020 - Proceedings*, 2020.

[25] Antonia Gambacorta, Mark Stephen, Fabrizio Gambini, Joseph Santanello, Priscilla Mohammed, Dan Sullivan, John Blaisdell, Robert Rosenberg, William Blumberg, Isaac Moradi, Yanqiu Zhu, Will McCarty, Joel Susskind, Paul Racette, and Jeffrey Piepmeier. The hyperspectral microwave photonic instrument (hympi) - advancing our understanding of the earth's planetary boundary layer from space. In *IGARSS 2022 - 2022 IEEE International Geoscience and Remote Sensing Symposium*, pages 4468–4471, 2022.

[26] D. N. Baker. The occurrence of operational anomalies in spacecraft and their relationship to space weather. *IEEE Transactions on Plasma Science*, 28(6):2007–2016, 2000.

[27] Sébastien Bourdarie and Michael Xapsos. The near-earth space radiation environment. *IEEE Transactions on Nuclear Science*, 55(4):1810–1832, 2008.

[28] R. H. Johnson, L. D. Montierth, J. R. Dennison, J. S. Dyer, and E. R. Lindstrom. Small-scale simulation chamber for space environment survivability testing. *IEEE Transactions on Plasma Science*, 41(12):3453–3458, 2013.

[29] M. Farzaneh, K. Maize, D. Lüeren, J. A. Summers, P. M. Mayer, P. E. Raad, K. P. Pipe, A. Shakouri, R. J. Ram, and Janice A. Hudgings. CCD-based thermoreflectance microscopy: Principles and applications. *Journal of Physics D: Applied Physics*, 42(14), 2009.

[30] M. Planck. *The Theory of Heat Radiation*. Blakiston, 1914.

[31] Lord Rayleigh. Remarks upon the law of complete radiation. *The London, Edinburgh, and Dublin Philosophical Magazine and Journal of Science*, 49(301):539–540, June 1900.

[32] J. B. Johnson. Thermal agitation of electricity in conductors. *Phys. Rev.*, 32:97–109, Jul 1928.

[33] G. Kirchhoff. Ueber das verhältniss zwischen dem emissionsvermögen und dem absorptionsvermögen der körper für wärme und licht. *Annalen der Physik und Chemie*, 185(2):275–301, 1860.

[34] C. E. Shannon. Communication in the presence of noise. *Proceedings of the IRE*, 37(1):10–21, 1949.

[35] F. N. Hooge. 1/f noise sources. *IEEE Transactions on Electron Devices*, 41(11):1926–1935, 1994.

[36] R. H. Dicke. The measurement of thermal radiation at microwave frequencies. *Review of Scientific Instruments*, 17(7):268–275, July 1946.

[37] William Emery and Adriano Camps. *Introduction to Satellite Remote Sensing*. Elsevier, 2017.

[38] Paul Vanden Bout. Interference and Radioastronomy. *Physics Today*, 44(11):41–49, 1991.

[39] A. Nothnagel, T. Artz, D. Behrend, and Z. Malkin. International VLBI Service for Geodesy and Astrometry: Delivering high-quality products and embarking on observations of the next generation. *Journal of Geodesy*, 91(7):711–721, jul 2017.

[40] John D. Kraus. *Radio Astronomy 2e*. Cygnus-Quasar Books, 1986.

[41] P. A. Fridman and W. A. Baan. Rfi mitigation methods in radio astronomy. *Astronomy & Astrophysics*, 378(1):327–344, October 2001.

[42] A. Niell, J. Barrett, A. Burns, R. Cappallo, B. Corey, M. Derome, C. Eckert, P. Elosegui, R. McWhirter, M. Poirier, G. Rajagopalan, A. Rogers, C. Ruszczyk, J. SooHoo, M. Titus, A. Whitney, D. Behrend, S. Bolotin, J. Gipson, D. Gordon, E. Himwich, and B. Petrachenko. Demonstration of a Broadband Very Long Baseline Interferometer System: A New Instrument for High-Precision Space Geodesy. *Radio Science*, 53(10):1269–1291, oct 2018.

[43] J. F. McGarry, E D Hoffman, J J Degnan, J W Cheek, C B Clarke, I F Diegel, H. L. Donovan, J E Horvath, M Marzouk, A R Nelson, D S Patterson, R L Ricklefs, M. D. Shappirio, S L Wetzel, and T W Zagwodzki. NASA's satellite laser ranging systems for the twenty-first century. *Journal of Geodesy*, 93(11):2249–2262, nov 2019.

[44] S. M. Merkowitz, S. Bolotin, P. Elosegui, J. Esper, J. Gipson, L. Hilliard, E. Himwich, E. D. Hoffman, D. D. Lakins, R. C. Lamb, F. G. Lemoine, J. L. Long, J. F. McGarry, D. S. MacMillan, B. P. Michael, C. Noll, E. C. Pavlis, M. R. Pearlman, C. Ruszczyk, M. D. Shappirio, and D. A. Stowers. Modernizing and expanding the NASA space geodesy network to meet future geodetic requirements. *Journal of Geodesy*, 93(11):2263–2273, October 2018.

[45] Annette Bussmann-Holder and Hugo Keller. High-temperature superconductors: underlying physics and applications. *Zeitschrift für Naturforschung B*, 75(1-2):3–14, 2020.

[46] S. Wallage, J. L. Tauritz, G. H. Tan, P. Hadley, and J. E. Mooij. High Tc superconducting CPW bandstop filters for radio astronomy front ends. *IEEE Transactions on Applied Superconductivity*, 7(2 PART 3):3489–3491, 1997.

[47] Haiwen Liu, Lingxin Rao, Yichen Xu, Pin Wen, Baoping Ren, Xuehui Guan, Yusheng He, Liang Sun, and Jun Ma. Design of High-Temperature Superconducting Wideband Bandpass Filter with Narrow-Band Notch Resonators for Radio Telescope Application. *IEEE Transactions on Applied Superconductivity*, 27(4):6–9, 2017.

[48] Yong Heng, Xubo Guo, Bisong Cao, Bin Wei, Xiaoping Zhang, Guoyong Zhang, and Xiaoke Song. Compact superconducting dual-band bandpass filter by combining bandpass and bandstop filters. *Electronics Letters*, 49(19):1230–1232, 2013.

[49] Srikanta Pal, Michael J. Lancaster, and Roger D. Norrod. HTS bandstop filter for radio astronomy. *IEEE Microwave and Wireless Components Letters*, 22(5):236–238, 2012.

[50] Paul D. Laforge, Raafat R. Mansour, and Ming Yu. The use of low-pass filters as impedance inverters for highly miniaturized superconducting bandstop filter designs. *IEEE Transactions on Applied Superconductivity*, 21(3 PART 1):575–578, 2011.

[51] A. Corona-Chavez, M. Nogues-Hoyos, L. Esteras-Otal, D. V.B. Murthy, and B. Sanchez-Rinza. A high-temperature superconducting notch filter to suppress cellular-band interference in radiotelescopes. *IEEE Transactions on Applied Superconductivity*, 21(2):68–70, 2011.

[52] Zaid Aboush and Adrian Porch. Compact, narrow bandwidth, lumped element bandstop resonators. *IEEE Microwave and Wireless Components Letters*, 15(8):524–526, 2005.

[53] B.A. Aminov, H. Piei, M.A. Hein, T. Kaiser, G. Muller, A. Baumfalk, H.J. Chaloupka, S. Kolesov, H. Medelius, and E. Wikborg. YBaCuO disk resonator filters operating at high power. *IEEE Transactions on Appiled Superconductivity*, 9(2):4185–4188, jun 1999.

[54] Xiaofeng He, Xueqiang Zhang, Yuehui Wang, Lu Gao, Jia Wang, Bin Cui, Yongbo Bian, Tao Yu, Qiang Zhang, Hong Li, Chunguang Li, Junjie Li, Changzhi Gu, and Yusheng He. An ultra-narrow band eight-pole dual-mode HTS patch filter. *Physica C: Superconductivity and its Applications*, 469(21):1925–1929, 2009.

[55] Takafumi Saito, Shun Kodama, Taiki Saito, Shigetoshi Ohshima, and Atsushi Saito. Design of High Power Handling Filter Using Cascaded Quadruplet Superconducting Bulk Resonators. *IEEE Transactions on Applied Superconductivity*, 28(4):4–7, 2018.

[56] Tianning Zheng, Bin Wei, Bisong Cao, Xubo Guo, Xiaoping Zhang, Dan Wang, Cheng Feng, Zhan Xu, and Zhaojiang Shang. Design of a High-Power Superconducting Filter with Novel DGS Structures. *IEEE Transactions on Applied Superconductivity*, 24(6), 2014.

[57] Masataka Ohira, Makoto Kanomata, Zhewang Ma, and Xiaolong Wang. A New Microstrip Bandstop Filter for Fully Canonical Cul-de-Sac Coupling Configuration. In *IEEE MTT-S International Microwave Symposium Digest*, volume 2018-June, pages 708–711. Institute of Electrical and Electronics Engineers Inc., aug 2018.

[58] Ting Zhang, Jia Du, and Y. Jay Guo. High-Tc Superconducting Microwave and Millimeter Devices and Circuits—An Overview. *IEEE Journal of Microwaves*, 2(3):374–388, 2022.

[59] Lu Gao, Liang Sun, Fei Li, Qiang Zhang, Yuehui Wang, Tao Yu, Jin Guo, Yongbo Bian, Chunguang Li, Xueqiang Zhang, Hong Li, Jibao Meng, and Yusheng He. 8-GHz narrowband high-temperature superconducting filter with high selectivity and flat group delay. *IEEE Transactions on Microwave Theory and Techniques*, 57(1):1767–1773, 2009.

[60] Tao Yu, Chunguang Li, Fei Li, Qiang Zhang, Liang Sun, Lu Gao, Yuehui Wang, Xueqiang Zhang, Hong Li, Chengjin Jin, Jianbin Li, Hongfei Liu, Changzheng Gao, Jibao Meng, and Yusheng He. A wideband superconducting filter using strong coupling resonators for radio astronomy observatory. *IEEE Transactions on Microwave Theory and Techniques*, 57(1):1783–1789, 2009.

[61] K.S. Kale. *High Temperature Superconducting Microwave Devices*. PhD thesis, University of Oxford, 1996.

[62] J. H. Takemoto, C. M. Jackson, H. M. Manasevit, D. C. St. John, J. F. Burch, K. P. Daly, and R. W. Simon. Microstrip resonators using two-sided metalorganic chemical vapor deposited er-ba-cu-o thin films. *Applied Physics Letters*, 58(10):1109–1111, March 1991.

[63] A. P. Jenkins. *Microwave applications of high temperature superconductors*. PhD thesis, University of Oxford, 1994. Copyright - Database copyright ProQuest LLC; ProQuest does not claim copyright in the individual underlying works; Analyte descriptor - Bibliographic data provided by EThOS, the British Library's UK thesis service: https://ethos.bl.uk/OrderDetails.do?uin=uk.bl.ethos.259904; Last updated - 2023-02-15.

[64] M. K. Wu, J. R. Ashburn, C. J. Torng, P. H. Hor, R. L. Meng, L. Gao, Z. J. Huang, Y. Q. Wang, and C. W. Chu. Superconductivity at 93 k in a new mixed-phase y-ba-cu-o compound system at ambient pressure. *Phys. Rev. Lett.*, 58:908–910, Mar 1987.

[65] C. W. Chu, J. Bechtold, L. Gao, P. H. Hor, Z. J. Huang, R. L. Meng, Y. Y. Sun, Y. Q. Wang, and Y. Y. Xue. Superconductivity up to 114 k in the bi-al-ca-sr-cu-o compound system without rare-earth elements. *Phys. Rev. Lett.*, 60:941–943, Mar 1988.

[66] C. W. Chu, L. Gao, F. Chen, Z. J. Huang, R. L. Meng, and Y. Y. Xue. Superconductivity above 150 k in hgba2ca2cu3o8 at high pressures. *Nature*, 365(6444):323–325, September 1993.

[67] S. S. P. Parkin, V. Y. Lee, A. I. Nazzal, R. Savoy, R. Beyers, and S. J. La Placa. Tl-ba-ca-cu-o: A new class of crystal structures exhibiting volume superconductivity at up to $\simeq$110 k. *Phys. Rev. Lett.*, 61:750–753, Aug 1988.

[68] Anant V. Narlikar, editor. *High Temperature Superconductivity 2*. Springer Berlin Heidelberg, 2004.

[69] Y. Hang, D. P. Fan, S. U. Zhang, H. C. Zhang, P. H. Wu, M. Qian, B. X. Jiang, Z. J. Sun, S. Z. Yang, and Z. M. Ji. In-situ preparation of YBCO thin films on single crystal LaAlO3. In *Advances in Superconductivity II*, pages 789–791. Springer Japan, 1990.

[70] M. Bauer, R. Semerad, and H. Kinder. YBCO films on metal substrates with biaxially aligned MgO buffer layers. *IEEE Transactions on Appiled Superconductivity*, 9(2):1502–1505, June 1999.

[71] E. Rozan, C. Collado, A. Garcia, J.M. O'Callaghan, R. Pous, L. Fabrega, J. Rius, R. Rubi, J. Fontcuberta, and F. Harackiewicz. Design and fabrication of coplanar YBCO structures on lithium niobate substrates. *IEEE Transactions on Appiled Superconductivity*, 9(2):2866–2869, June 1999.

[72] J. C. Sabataitis, C. H. Mueller, F. A. Miranda, J. Warner, and K. B. Bhasin. YBCO high-temperature superconducting filters on m-plane sapphire substrates. In *A Cryogenic Engineering Conference Publication*, pages 1755–1760. Springer US, 1996.

[73] Fumihiko Aiga, Hiroyuki Fuke, Yoshiaki Terashima, Mutsuki Yamazaki, Hiroyuki Kayano, and Tatsunori Hashimoto. HTS hairpin microstrip filter on r-cut sapphire substrate. *IEEE Transactions on Applied Superconductivity*, 13(2 I):287–290, 2003.

[74] R. Levy and S.B. Cohn. A history of microwave filter research, design, and development. *IEEE Transactions on Microwave Theory and Techniques*, 32(9):1055–1067, 1984.

[75] G. L. Matthaei, L. Young, and Jones E.N.T. Microwave filters, impedance matching networks and coupling structure. *Norwood, MA, Artech House*, 1980.

[76] D. M. Pozar. *Microwave engineering; 4th ed.* Wiley, Hoboken, NJ, 2011.

[77] Jia-Sheng. Hong and M. J. Lancaster. *Microstrip Filters for RF / Microwave*, volume 7. Wiley, 2001.

[78] D. C. Mattis and J. Bardeen. Theory of the anomalous skin effect in normal and superconducting metals. *Phys. Rev.*, 111:412–417, Jul 1958.

[79] Jia-Sheng Hong, M.J. Lancaster, R.B. Greed, Daniel Voyce, Dieter Jedamzik, J.A. Holland, H.J. Chaloupka, and J.-C. Mage. Thin film HTS passive microwave components for advanced communication systems. *IEEE Transactions on Appiled Superconductivity*, 9(2):3893–3896, jun 1999.

[80] M. Esmaeili and J. Bornemann. Microstrip bandstop filters using L- and T-shaped resonators. In *2015 Asia-Pacific Microwave Conference (APMC)*, volume 0, pages 1–3. IEEE, dec 2015.

[81] Guoyong Zhang, Michael J. Lancaster, Frederick Huang, and Neil Roddis. A superconducting microstrip bandstop filter for an L-band radio telescope receiver. *35th European Microwave Conference 2005 - Conference Proceedings*, 1:697–700, 2005.

[82] David Marpaung, Chris Roeloffzen, René Heideman, Arne Leinse, Salvador Sales, and José Capmany. Integrated microwave photonics. *Laser & Photonics Reviews*, 7(4):506–538, January 2013.

[83] Pradip Gatkine, Sylvain Veilleux, John Mather, Christopher Betters, Jonathan Bland-Hawthorn, Julia Bryant, S. Bradley Cenko, Mario Dagenais, Drake Deming, Simon Ellis, Matthew Greenhouse, Andrew Harris, Nemanja Jovanovic, Steve Kuhlmann, Alexander Kutyrev, Sergio Leon-Saval, Kalaga Madhav, Samuel Moseley, Barnaby Norris, Bernard Rauscher, Martin Roth, and Stuart Vogel. Astro2020: Astrophotonics white paper, 2019.

[84] Anthony C. Lindsay, Geoff A. Knight, and Stephen T. Winnall. Photonic Mixers for Wide Bandwidth RF Receiver Applications. *IEEE Transactions on Microwave Theory and Techniques*, 43(9):2311–2317, 1995.

[85] Christian D. Kummerow, Joseph C. Poczatek, Scott Almond, Wesley Berg, Olivia Jarrett, Andrew Jones, Michael Kantner, and Chia Pang Kuo. Hyperspectral Microwave Sensors-Advantages and Limitations. *IEEE Journal of Selected Topics in Applied Earth Observations and Remote Sensing*, 15:764–775, 2022.

[86] Virginia Diodes, Inc. Vdi. `http://www.vadiodes.com/`. [Accessed 07-Aug-2023].

[87] Yan Zhang, Yanghyo Kim, Adrian Tang, Jonathan H. Kawamura, Theodore J. Reck, and Mau-Chung Frank Chang. Integrated wide-band CMOS spectrometer systems for spaceborne telescopic sensing. *IEEE Transactions on Circuits and Systems I: Regular Papers*, 66(5):1863–1873, May 2019.

[88] V. I. Pustovoit. Acousto-optical spectrometers. In *Optical Society of America Annual Meeting*. Optica Publishing Group, 1990.

[89] P. Hartogh and G. K. Hartmann. A high-resolution chirp transform spectrometer for microwave measurements. *Measurement Science and Technology*, 1(7):592, jul 1990.

[90] F. Hsiao, A. Tang, Y. Kim, Brian Drouin, Goutam Chattopadhyay, and M-C Frank Chang. A 2.2 gs/s 188mw spectrometer processor in 65nm cmos for supporting low-power thz planetary instruments. In *2015 IEEE Custom Integrated Circuits Conference (CICC)*, pages 1–3, 2015.

[91] The swas spacecraft. `https://lweb.cfa.harvard.edu/swas/spacecraft.html`. [Accessed 01-08-2023].

[92] H. L. Nordh, F. von Schéele, U. Frisk, K. Ahola, R. S. Booth, P. J. Encrenaz, Å. Hjalmarson, D. Kendall, E. Kyrölä, S. Kwok, A. Lecacheux, G. Leppelmeier, E. J. Llewellyn, K. Mattila, G. Mégie, D. Murtagh, M. Rougeron, and G. Witt. The odin orbital observatory. *Astronomy & Astrophysics*, 402(3):L21–L25, April 2003.

[93] S. Gulkis, M. Frerking, J. Crovisier, G. Beaudin, P. Hartogh, P. Encrenaz, T. Koch, C. Kahn, Y. Salinas, R. Nowicki, R. Irigoyen, M. Janssen, P. Stek, M. Hofstadter, M. Allen, C. Backus, L. Kamp, C. Jarchow, E. Steinmetz, A. Deschamps, J. Krieg, M. Gheudin, D. Bockelée-Morvan, N. Biver, T. Encrenaz, D. Despois, W. Ip, E. Lellouch, I. Mann, D. Muhleman, H. Rauer, P. Schloerb, and T. Spilker. MIRO: Microwave instrument for rosetta orbiter. *Space Science Reviews*, 128(1-4):561–597, November 2006.

[94] J.W. Waters, L. Froidevaux, R.S. Harwood, R.F. Jarnot, H.M. Pickett, W.G. Read, P.H. Siegel, R.E. Cofield, M.J. Filipiak, D.A. Flower, J.R. Holden, G.K. Lau, N.J. Livesey, G.L. Manney, H.C. Pumphrey, M.L. Santee, D.L. Wu, D.T. Cuddy, R.R. Lay, M.S. Loo, V.S. Perun, M.J. Schwartz, P.C. Stek, R.P. Thurstans, M.A. Boyles, K.M. Chandra, M.C. Chavez, Gun-Shing Chen, B.V. Chudasama, R. Dodge, R.A. Fuller, M.A. Girard, J.H. Jiang, Yibo Jiang, B.W. Knosp, R.C. LaBelle, J.C. Lam, K.A. Lee, D. Miller, J.E. Oswald, N.C. Patel, D.M. Pukala, O. Quintero, D.M. Scaff, W. Van Snyder, M.C. Tope, P.A. Wagner, and M.J. Walch. The earth observing system microwave limb sounder (eos mls) on the aura satellite. *IEEE Transactions on Geoscience and Remote Sensing*, 44(5):1075–1092, 2006.

[95] Ken ichi Kikuchi, Toshiyuki Nishibori, Satoshi Ochiai, Hiroyuki Ozeki, Yoshihisa Irimajiri, Yasuko Kasai, Makoto Koike, Takeshi Manabe, Kazuo Mizukoshi, Yasuhiro Murayama, Tomoo Nagahama, Takuki Sano, Ryota Sato, Masumichi Seta, Chikako Takahashi, Masahiro Takayanagi, Harunobu Masuko, Junji Inatani, Makoto Suzuki, and Masato Shiotani. Overview and early results of the superconducting submillimeter-wave limb-emission sounder (SMILES). *Journal of Geophysical Research*, 115(D23), December 2010.

[96] P. Hartogh, S. Barabash, G. Beaudin, P. Börner, D. Bockeleé-Morvan, W. Boogaerts, T. Cavalié, U. R. Christensen, A. Dannenberg, P. Eriksson, M. Fränz, T. Fouchet, U. Frisk,

K. Hocke, C. Janssen, C. Jarchow, Y. Kasai, K. Kikuchi, J. M. Krieg, N. Krupp, T. Kuroda, E. Lellouch, A. Loose, A. Maestrini, T. Manabe, A. S. Medvedev, J. Mendrok, E. P. Miettinen, R. Moreno, A. Murk, D. Murtagh, T. Nishibori, M. Rengel, L. Rezac, H. Sagawa, E. Steinmetz, B. Thomas, J. Urban, and J. Wicht. The Submillimetre Wave Instrument on JUICE. In *European Planetary Science Congress*, pages EPSC2013–710, September 2013.

[97] Gary J. Melnick, John R. Stauffer, Matthew L. N. Ashby, Edwin A. Bergin, Gordon Chin, Neal R. Erickson, Paul F. Goldsmith, Martin Harwit, John E. Howe, Steven C. Kleiner, David G. Koch, David A. Neufeld, Brian M. Patten, René Plume, Rudolf Schieder, Ronald L. Snell, Volker Tolls, Zhong Wang, Gisbert Winnewisser, and Yun Fei Zhang. The [ITAL]submillimeter wave astronomy satellite[/ITAL]: Science objectives and instrument description. *The Astrophysical Journal*, 539(2):L77–L85, August 2000.

[98] U. Frisk, M. Hagström, J. Ala-Laurinaho, S. Andersson, J.-C. Berges, J.-P. Chabaud, M. Dahlgren, A. Emrich, H.-G. Florén, G. Florin, M. Fredrixon, T. Gaier, R. Haas, T. Hirvonen, Å. Hjalmarsson, B. Jakobsson, P. Jukkala, P. S. Kildal, E. Kollberg, J. Lassing, A. Lecacheux, P. Lehikoinen, A. Lehto, J. Mallat, C. Marty, D. Michet, J. Narbonne, M. Nexon, M. Olberg, A. O. H. Olofsson, G. Olofsson, A. Origné, M. Petersson, P. Piironen, R. Pons, D. Pouliquen, I. Ristorcelli, C. Rosolen, G. Rouaix, A. V. Räisänen, G. Serra, F. Sjöberg, L. Stenmark, S. Torchinsky, J. Tuovinen, C. Ullberg, E. Vinterhav, N. Wadefalk, H. Zirath, P. Zimmermann, and R. Zimmermann. The odin satellite. *Astronomy & Astrophysics*, 402(3):L27–L34, April 2003.

[99] Karl Jacob, Axel Murk, Hyunjoo Kim, Peter Sobis, Anders Emrich, Vladimir Drakinskiy, Jan Stake, Alain Maestrini, Jeanne Treuttel, Ferhat Tamazouzt, Bertrand Thomas, Martin Philipp, and Paul Hartogh. Characterization of the 530-625 GHz receiver unit for the Jupiter mission JUICE/SWI. In *Proceedings of the 36th ESA Antenna Workshop on Antennas and RF Systems for Space Science*, 2015.

[100] João Teixeira, Jeffrey R Piepmeier, Amin R Nehrir, Chi O Ao, Shuyi S Chen, Carol A Clayson, Ann M Fridlind, Matthew Lebsock, Will Mccarty, Haydee Salmun, Joseph A Santanello, David D Turner, Zhien Wang, and Xubin Zeng. Toward a Global Planetary Boundary Layer Observing System: The NASA PBL Incubation Study Team Report. *NASA PBL Incubation Study Team*, 134 pp., 2021.

[101] Todd Pett, Jennifer H. Lee, Yossef Ehrlichman, Hayk Gevorgyan, Anatol Khilo, and Miloš Popović. Photonics-based Microwave Radiometer for Hyperspectral Earth Remote Sensing. *MWP 2018 - 2018 International Topical Meeting on Microwave Photonics*, 2018.

[102] Christopher A. Schuetz, Janusz Murakowski, Garrett J. Schneider, and Dennis W. Prather. Radiometric millimeter-wave detection via optical upconversion and carrier suppression. *IEEE Transactions on Microwave Theory and Techniques*, 53(5):1732–1738, 2005.

[103] Thomas Dillon, Christopher Schuetz, Andrew Wright, Stephen Kozacik, Zachary El-Azom, Shouyuan Shi, Dennis Prather, and Adam Rutkowski. Compact passive millimeter wave imager for degraded visual and GPS-denied navigation. *2019 IEEE Research and*

Applications of Photonics in Defense Conference, RAPID 2019 - Proceedings, pages 19–22, 2019.

[104] Gabriel Santamaría Botello, Florian Sedlmeir, Alfredo Rueda, Kerlos Atia Abdalmalak, Elliott R. Brown, Gerd Leuchs, Sascha Preu, Daniel Segovia-Vargas, Dmitry V. Strekalov, Luis Enrique García Muñoz, and Harald G. L. Schwefel. Sensitivity limits of millimeter-wave photonic radiometers based on efficient electro-optic upconverters. *Optica*, 5(10):1210, 2018.

[105] Enrique Nova, Jordi Romeu, Santiago Capdevila, Francesc Torres, and Lluis Jofre. Optical signal processor for millimeter-wave interferometric radiometry. *IEEE Transactions on Geoscience and Remote Sensing*, 52(5):2357–2368, 2014.

[106] Cheng Wang, Mian Zhang, Xi Chen, Maxime Bertrand, Amirhassan Shams-Ansari, Sethumadhavan Chandrasekhar, Peter Winzer, and Marko Lončar. Integrated lithium niobate electro-optic modulators operating at CMOS-compatible voltages. *Nature*, 562(7725):101–104, 2018.

[107] Steven T. Lipkowitz, Timothy U. Horton, and Thomas E. Murphy. Wideband microwave electro-optic image rejection mixer. *Optics Letters*, 44(19):4710, 2019.

[108] Yunxin Wang, Jingnan Li, Tao Zhou, Dayong Wang, Jiahao Xu, Xin Zhong, Dengcai Yang, and Lu Rong. All-Optical Microwave Photonic Downconverter with Tunable Phase Shift. *IEEE Photonics Journal*, 9(6), 2017.

[109] G. K. Gopalakrishnan, M. M. Howerton, R. P. Moeller, W. K. Burns, K. J. Williams, and R. D. Esman. A Low-Loss Downconverting Analog Fiber-Optic Link. *IEEE Transactions on Microwave Theory and Techniques*, 43(9):2318–2323, 1995.

[110] Vincent R. Pagán, Bryan M. Haas, and T. E. Murphy. Linearized electrooptic microwave downconversion using phase modulation and optical filtering. *Optics Express*, 19(2):883, jan 2011.

[111] C. Lanczos and B. Gellai. Fourier analysis of random sequences. *Computers & Mathematics with Applications*, 1(3-4):269–276, 1975.

[112] Jared A. Grauer. Random noise generation using fourier series. *Journal of Aircraft*, 55(4):1753–1759, 2018.

[113] Vincent J. Urick, Jason D. Mckinney, and Keith J. Williams. *Fundamentals of Microwave Photonics*. John Wiley & Sons, Inc, February 2015.

[114] Frank Bucholtz, Matthew J Mondich, Joseph M Singley, Jason D Mckinney, and Keith J Williams. The Noise Figure of Analog RF Photonic Receivers: Simple Links, WDM Links, and WDM Receive-Mode Beamformers. *Naval Research Laboratory*, 2020.

[115] Freedom Photonics LLC, a Luminar Company. Freedom photonics. `http://www.freedomphotonics.com/`. [Accessed 07-Aug-2023].

[116] Amanda N. Bozovich. Photonic integrated circuits (pics) for next generation space applications. In *Electronics Technology Workshop*. NASA Electronic Parts and Packaging (NEPP) Program, 2020.

[117] Kishore Padmaraju, Johnnie Chan, Long Chen, Michal Lipson, and Keren Bergman. Thermal stabilization of a microring modulator using feedback control. *Optics Express*, 20(27):27999, December 2012.

[118] Stefano Biasi, Riccardo Franchi, Davide Bazzanella, and Lorenzo Pavesi. On the effect of the thermal cross-talk in a photonic feed-forward neural network based on silicon microresonators. *Frontiers in Physics*, 10, December 2022.

[119] N. Lindenmann, G. Balthasar, D. Hillerkuss, R. Schmogrow, M. Jordan, J. Leuthold, W. Freude, and C. Koos. Photonic wire bonding: a novel concept for chip-scale interconnects. *Optics Express*, 20(16):17667, 2012.

[120] Bahram Jalali and Sasan Fathpour. Silicon photonics. *J. Lightwave Technol.*, 24(12):4600–4615, Dec 2006.

[121] Tom Baehr-Jones, Thierry Pinguet, Patrick Lo Guo-Qiang, Steven Danziger, Dennis Prather, and Michael Hochberg. Myths and rumours of silicon photonics. *Nature Photonics*, 6(4):206–208, March 2012.

[122] Meint Smit, Xaveer Leijtens, Huub Ambrosius, Erwin Bente, Jos van der Tol, Barry Smalbrugge, Tjibbe de Vries, Erik-Jan Geluk, Jeroen Bolk, Rene van Veldhoven, Luc Augustin, Peter Thijs, Domenico D'Agostino, Hadi Rabbani, Katarzyna Lawniczuk, Stanislaw Stopinski, Saeed Tahvili, Antonio Corradi, Emil Kleijn, Dzmitry Dzibrou, Manuela Felicetti, Elton Bitincka, Valentina Moskalenko, Jing Zhao, Rui Santos, Giovanni Gilardi, Weiming Yao, Kevin Williams, Patty Stabile, Piet Kuindersma, Josselin Pello, Srivathsa Bhat, Yuqing Jiao, Dominik Heiss, Gunther Roelkens, Mike Wale, Paul Firth, Francisco Soares, Norbert Grote, Martin Schell, Helene Debregeas, Mohand Achouche, Jean-Louis Gentner, Arjen Bakker, Twan Korthorst, Dominic Gallagher, Andrew Dabbs, Andrea Melloni, Francesco Morichetti, Daniele Melati, Adrian Wonfor, Richard Penty, Ronald Broeke, Bob Musk, and Dave Robbins. An introduction to InP-based generic integration technology. *Semiconductor Science and Technology*, 29(8):083001, June 2014.

[123] Mian Zhang, Cheng Wang, Prashanta Kharel, Di Zhu, and Marko Lončar. Integrated lithium niobate electro-optic modulators: when performance meets scalability. *Optica*, 8(5):652–667, May 2021.

[124] Zhen Sheng, Liu Liu, Joost Brouckaert, Sailing He, and Dries Van Thourhout. Ingaas pin photodetectors integrated on silicon-on-insulator waveguides. *Opt. Express*, 18(2):1756–1761, Jan 2010.

[125] David Marpaung, Jianping Yao, and José Capmany. Integrated microwave photonics. *Nature Photonics*, 13(2):80–90, January 2019.

[126] A. Yeniay, R. Gao, K. Takayama, R. Gao, and A.F. Garito. Ultra-low-loss polymer waveguides. *Journal of Lightwave Technology*, 22(1):154–158, January 2004.

[127] S. J. Madden, D-Y. Choi, D. A. Bulla, A. V. Rode, B. Luther-Davies, V. G. Ta'eed, M. D. Pelusi, and B. J. Eggleton. Long, low loss etched as_2s_3 chalcogenide waveguides for all-optical signal regeneration. *Optics Express*, 15(22):14414, 2007.

[128] Tin Komljenovic, Michael Davenport, Jared Hulme, Alan Y. Liu, Christos T. Santis, Alexander Spott, Sudharsanan Srinivasan, Eric J. Stanton, Chong Zhang, and John E. Bowers. Heterogeneous silicon photonic integrated circuits. *Journal of Lightwave Technology*, 34(1):20–35, January 2016.

[129] Martijn J. R. Heck, Jared F. Bauters, Michael L. Davenport, Jonathan K. Doylend, Siddharth Jain, Geza Kurczveil, Sudharsanan Srinivasan, Yongbo Tang, and John E. Bowers. Hybrid silicon photonic integrated circuit technology. *IEEE Journal of Selected Topics in Quantum Electronics*, 19(4):6100117–6100117, July 2013.

[130] Chris G. H. Roeloffzen, Marcel Hoekman, Edwin J. Klein, Lennart S. Wevers, Roelof Bernardus Timens, Denys Marchenko, Dimitri Geskus, Ronald Dekker, Andrea Alippi, Robert Grootjans, Albert van Rees, Ruud M. Oldenbeuving, Jorn P. Epping, Rene G. Heideman, Kerstin Worhoff, Arne Leinse, Douwe Geuzebroek, Erik Schreuder, Paulus W. L. van Dijk, Ilka Visscher, Caterina Taddei, Youwen Fan, Caterina Taballione, Yang Liu, David Marpaung, Leimeng Zhuang, Meryem Benelajla, and Klaus-J. Boller. Low-loss si3n4 TriPleX optical waveguides: Technology and applications overview. *IEEE Journal of Selected Topics in Quantum Electronics*, 24(4):1–21, July 2018.

[131] Muhammad Rodlin Billah, Matthias Blaicher, Tobias Hoose, Philipp-Immanuel Dietrich, Pablo Marin-Palomo, Nicole Lindenmann, Aleksandar Nesic, Andreas Hofmann, Ute Troppenz, Martin Moehrle, Sebastian Randel, Wolfgang Freude, and Christian Koos. Hybrid integration of silicon photonics circuits and inp lasers by photonic wire bonding. *Optica*, 5(7):876–883, Jul 2018.

[132] E. Matatagui, A. G. Thompson, and Manuel Cardona. Thermoreflectance in semiconductors. *Physical Review*, 176(3):950–960, 1968.

[133] Xu Xie, Kexin Yang, Dongyao Li, Tsung Han Tsai, Jungwoo Shin, Paul V. Braun, and David G. Cahill. High and low thermal conductivity of amorphous macromolecules. *Physical Review B*, 95(3):1–9, 2017.

[134] Mingkang Wang, Georg Ramer, Diego J. Perez-Morelo, Georges Pavlidis, Jeffrey J. Schwartz, Liya Yu, Robert Ilic, Vladimir A. Aksyuk, and Andrea Centrone. High Throughput Nanoimaging of Thermal Conductivity and Interfacial Thermal Conductance. *Nano Letters*, 22(11):4325–4332, 2022.

[135] Zhong G. Ling, Kun Lian, and Linke Jian. Improved patterning quality of SU-8 microstructures by optimizing the exposure parameters. *Advances in Resist Technology and Processing XVII*, 3999(June 2000):1019, 2000.

[136] Vanguard Automation GmbH. Photonic multi-chip integration from Vanguard Automation. http://www.vanguard-automation.com/. [Accessed 28-Jun-2023].

[137] Kayaku Materials. SU-8 2000 Permanent Negative Epoxy Photoresist. http://kayakuam.com/products/su-8-2000/. [Accessed 28-Jun-2023].

[138] M Farzaneh, K Maize, D Lüerßen, J A Summers, P M Mayer, P E Raad, K P Pipe, A Shakouri, R J Ram, and Janice A Hudgings. Ccd-based thermoreflectance microscopy: principles and applications. *Journal of Physics D: Applied Physics*, 42(14):143001, jun 2009.

[139] V. G. Garcia and M. Farzaneh. Transient thermal imaging of a vertical cavity surface-emitting laser using thermoreflectance microscopy. *Journal of Applied Physics*, 119(4):045105, January 2016.

[140] B. Vermeersch, J. Christofferson, K. Maize, A. Shakouri, and G. De Mey. Time and frequency domain CCD-based thermoreflectance techniques for high-resolution transient thermal imaging. In *2010 26th Annual IEEE Semiconductor Thermal Measurement and Management Symposium (SEMI-THERM)*. IEEE, February 2010.

[141] J. Christofferson, Y. Ezzahri, K. Maize, and A. Shakouri. Transient thermal imaging of pulsed-operation superlattice micro-refrigerators. In *2009 25th Annual IEEE Semiconductor Thermal Measurement and Management Symposium*. IEEE, 2009.

[142] K. Maize, Christofferson J, and A. Shakouri. Transient thermal imaging using thermoreflectance. In *2008 Twenty-fourth Annual IEEE Semionductor Thermal Measurement and Management Symposium*. IEEE, March 2008.

[143] Corey M. Rountree, Pradeep Kumar Ramkumar, and Laxman Saggere. Novel imaging technique for non-destructive metrology and characterization of ultraviolet-sensitive polymeric microstructures. *Review of Scientific Instruments*, 91(3), 2020.

[144] Gilles Tessier, Sabrina Pavageau, Benoit Charlot, Celine Filloy, Daniele Fournier, B. Cretin, S. Dilhaire, S. Gomes, N. Trannoy, P. Vairac, and S. Volz. Quantitative thermoreflectance imaging: Calibration method and validation on a dedicated integrated circuit. *IEEE Transactions on Components and Packaging Technologies*, 30(4):604–608, December 2007.

[145] Maciej Bugajski, Tomasz Piwoński, Dorota Wawer, Tomasz Ochalski, Eckard Deichsel, Peter Unger, and Brian Corbett. Thermoreflectance study of facet heating in semiconductor lasers. *Materials Science in Semiconductor Processing*, 9(1-3):188–197, February 2006.

[146] Dustin Kendig, Kazuaki Yazawa, and Ali Shakouri. Thermal imaging of encapsulated LEDs. In *2011 27th Annual IEEE Semiconductor Thermal Measurement and Management Symposium*. IEEE, March 2011.

[147] Minerva Robles-Agudo, Martha Patricia Gonzalez-Tejeda, Porfirio Esau Martinez-Muñoz, and Ignacio Rojas-Rodríguez. Analysis of the absorption phenomenon through the use of finite element method. In Maaz Khan, Gustavo Morari do Nascimento, and Marwa

El-Azazy, editors, *Modern Spectroscopic Techniques and Applications*, chapter 4. IntechOpen, Rijeka, 2019.

[148] Xingyu Zhang, Amir Hosseini, Xiaohui Lin, Harish Subbaraman, and Ray T. Chen. Polymer-based hybrid-integrated photonic devices for silicon on-chip modulation and board-level optical interconnects. *IEEE Journal of Selected Topics in Quantum Electronics*, 19(6):196–210, 2013.

[149] Cheng-Ling Lee, Rui-Cheng Zeng, Chun-Ren Yang, Chi-Feng Lin, Chao-Tsung Ma, and Wen-Fung Liu. Tapered polymer fiber inclinometers. *IEEE Photonics Journal*, 12(3):1–10, 2020.

[150] Abhai Kumar, Siddharth Nambiar, Rakshitha Kallega, Praveen Ranganath, Priya Ea, and Shankar Kumar Selvaraja. High-efficiency vertical fibre-to-polymer waveguide coupling scheme for scalable polymer photonic circuits. *Opt. Express*, 29(7):9699–9710, Mar 2021.

[151] Tara Fortier and Esther Baumann. 20 years of developments in optical frequency comb technology and applications. *Communications Physics*, 2(1), December 2019.

[152] Amirhassan Shams-Ansari, Dylan Renaud, Rebecca Cheng, Linbo Shao, Lingyan He, Di Zhu, Mengjie Yu, Hannah R. Grant, Leif Johansson, Mian Zhang, and Marko Lončar. Electrically pumped high power laser transmitter integrated on thin-film lithium niobate. *Optics InfoBase Conference Papers*, 9(4):408–411, 2022.